A&A, 710, A367 (2026)
https://doi.org/10.1051/0004-6361/202557418

Astronomy & Astrophysics

SN 2021lwz: Another exotic, luminous, and fast-evolving optical stripped-envelope supernova?

F. Poidevin[1,2,★], S. L. West[3], C. M. B. Omand[4], R. Könyves-Tóth[5,6,7], S. Schulze[8], L. Yan[19], T. Kangas[10,11], I. Pérez-Fournon[1,2], S. Geier[1,12], J. Sollerman[3], P. J. Pessi[3], C. M. Gutiérrez[1,2], T.-W. Chen[9], K.-R. Hinds[4], R. Marques-Chaves[13], R. Shirley[14], C. Jimenez Angel[1,2,12], R. Lunnan[3], D. A. Perley[4], N. Sarin[15,16], Y. Yao[17,18], R. Dekany[19], J. Purdum[19], A. Wold[20], R. R. Laher[20], M. J. Graham[21], M. M. Kasliwal[21], and T. Jegou Du Laz[22]

1 Instituto de Astrofísica de Canarias, Vía Láctea, 38205 La Laguna, Tenerife, Spain
2 Universidad de La Laguna, Departamento de Astrofísica, 38206 La Laguna, Tenerife, Spain
3 The Oskar Klein Centre, Department of Astronomy, Stockholm University, AlbaNova, SE-10691 Stockholm, Sweden
4 Astrophysics Research Institute, Liverpool John Moores University, Liverpool Science Park IC2, 146 Brownlow Hill, Liverpool L3 5RF, UK
5 Konkoly Observatory, CSFK, Konkoly-Thege M. út 15-17, Budapest 1121, Hungary
6 Department of Optics & Quantum Electronics, University of Szeged, Dóm tér 9, Szeged 6720, Hungary
7 ELTE Evös Loránd University, Gothard Astrophysical Observatory, 9700 Szombathely Szent Imre h. u. 112, Hungary
8 Center for Interdisciplinary Exploration and Research in Astrophysics (CIERA), Northwestern University, 1800 Sherman Ave, Evanston, IL 60201, USA
9 Graduate Institute of Astronomy, National Central University, 300 Jhongda Road, 32001 Jhongli, Taiwan
10 Finnish Centre for Astronomy with ESO (FINCA), FI-20014 University of Turku, Finland
11 Department of Physics and Astronomy, FI-20014 University of Turku, Finland
12 GRANTECAN, Cuesta de San José s/n, 38712 Breña Baja, La Palma, Spain
13 Geneva Observatory, University of Geneva, Chemin Pegasi 51, CH-1290 Versoix, Switzerland
14 Max-Planck-Institut für extraterrestrische Physik, Giessenbachstr. 1, 85748 Garching, Germany
15 Kavli Institute for Cosmology, University of Cambridge, Madingley Road, CB3 0HA Cambridge, UK
16 Institute of Astronomy, University of Cambridge, Madingley Road, CB3 0HA Cambridge, UK
17 Miller Institute for Basic Research in Science, 206B Stanley Hall, Berkeley, CA 94720, USA
18 Department of Astronomy, University of California, Berkeley, CA 94720-3411, USA
19 Caltech Optical Observatories, California Institute of Technology, Pasadena, CA 91125, USA
20 IPAC, California Institute of Technology, 1200 E. California, Blvd, Pasadena, CA 91125, USA
21 Division of Physics, Mathematics, and Astronomy, California Institute of Technology, Pasadena, CA 91125, USA
22 Cahill Center for Astrophysics, California Institute of Technology, MC 249-17, 1200 E California Boulevard, Pasadena, CA 91125, USA

Received 25 September 2025 / Accepted 20 March 2026

ABSTRACT

Context. Current large-scale, high-cadence surveys, such as the *Zwicky* Transient Facility (ZTF), provide detections of new and rare types of transients and supernovae (SNe) whose physical origins are not well understood.
Aims. We aim to investigate the nature of SN 2021lwz at a redshift $z = 0.065$, an over-luminous SN with an absolute magnitude of $M_g \sim -20.1$ AB that falls in the lower range of superluminous supernovae (SLSNe) luminosities and was discovered in a faint dwarf galaxy with an absolute magnitude of $M_g \simeq -14.5$ AB.
Methods. We studied SN 2021lwz using optical spectroscopy and photometry and by imaging linear polarimetry obtained during several follow-up campaigns. All the data were used to analyse and model the evolution of the explosion. Comparisons with other SNe of well-known or rarer types were investigated.
Results. SN 2021lwz belongs to the rare class of rapidly evolving transients. The bolometric light curve rises in about seven days to a peak luminosity of about 5×10^{43} erg/s, at a rate of 0.2 mag day^{-1} close to the peak. Spectroscopy modelling reveals more similarities with a normal Type Ic-like SN than with an SLSN before peak, showing slightly broadened lines after peak. Light curve modelling shows that the Arnett model of the bolometric light curve using a radioactive source (^{56}Ni) is not able to reasonably explain the light curve evolution. A magnetar model seems more appropriate, suggesting that the explosion of low ejecta mass ($M_{\rm ej} \sim 0.24\, M_\odot$) took place in a low-mass ($M \sim 10^{6.66}\, M_\odot$) dwarf galaxy of specific star formation rate about ten times larger than typical star-forming galaxies.
Conclusions. SN 2021lwz is an uncommon transient showing many similarities with several classes of transients, including rare transients. It may be an interesting example of how differences in ejecta mass and engine parameters could produce a wide range of engine-driven stripped-envelope SNe.

Key words. stars: magnetars – supernovae: general – supernovae: individual: SN 2021lwz – galaxies: dwarf

★ Corresponding author: fpoidevin@iac.es

1. Introduction

The advent of large-scale, high-cadence surveys such as the Catalina Real-Time Transient Survey (CRTS; Drake et al. 2009), the Panoramic Survey Telescope and Rapid Response System (Pan-STARRS; Kaiser et al. 2010), the Palomar Transient Factory (PTF; see Rau et al. 2009), the *Zwicky* Transient Facility (ZTF; Bellm et al. 2019b; Graham et al. 2019), and the Asteroid Terrestrial-impact Last Alert System (ATLAS; Tonry et al. 2018a), developed over the last two decades, have opened the possibility to detect new types of transients. They have been useful to start populating the parameter space of the rising time, $T_{\rm rise}$, defined as the time between the explosion and peak magnitude versus the absolute magnitude at peak ($M_{\rm abs}$) with new populations of objects. Among those, superluminous supernovae (SLSNe) are explosions expected to originate from core-collapsing stars. Such explosions may be forming a newborn rotating neutron star (Ostriker & Gunn 1971), or a magnetar (Kasen & Bildsten 2010; Woosley 2010). Interactions between the explosion products and the circumstellar medium (CSM) from previous progenitor mass loss is an additional mechanism often considered to interpret the diversity of light curves of H-poor SLSNe (e.g. Hosseinzadeh et al. 2022). An SLSN has often been considered as a type of stellar explosion that exhibits a peak luminosity ten or more times higher than that of a typical supernova (SN). This definition is quite general. In practice H-poor SLSNe are detected with absolute r-band magnitudes lying between ∼−22.5 and ∼−19.2 magnitudes (Gomez et al. 2024). The light curves of the largest sample from the ZTF (78 SLSNe) evolve slowly with a mean rest frame rise time of 41.9 ± 17.8 days (see Chen et al. 2023a,b), while Gomez et al. (2024) derived a mean rise time of 27^{+25}_{-13} days on a larger sample. In both distributions low-luminosity (∼20 mag), extremely fast rising (<10 days) transients are rare. From the ZTF sample, with a rising time of ∼10 days, and an absolute magnitude peaking close to $M_g = -21$, SN 2018bgv was the fastest SLSN observed by ZTF during the first months of the survey (Lunnan et al. 2020).

The formation of stars as single objects, or in binary and even triple-star systems – which is followed by their evolution up to a final stage (e.g. core collapse or disruptive events) – suggest the existence of a complex diversity of star evolution channels. Stars evolving in binary systems are subject to strong interactions with their environment (e.g. binary star companion, black-hole proximity, winds, shock waves) potentially leading to new types of transients. As such, a variety of new types of transients were recently discovered, including luminous fast blue optical transients (LFBOTs) such as AT 2018cow (the Cow) and AT 2020xnd (the Camel; see, e.g. Perley et al. 2021a; Ho et al. 2023, and references therein) and ultra-stripped supernovae (USSNe) such as SN 2014ft (or iPTF 14gqr) and SN 2019ehk (see, e.g. De et al. 2018; Nakaoka et al. 2021, and references therein). A more general term encompassing these events is 'rapidly evolving transients' (RETs; e.g. Drout et al. 2014; Arcavi et al. 2016; Tanaka et al. 2016; Pursiainen et al. 2018). Ideally, each of these types would be filling a given area in the phase space ($T_{\rm rise}$, $M_{\rm abs}$), but in practice distinct populations sometimes fill similar areas leading to a degeneracy in this parameter space, and more data-driven information is required. This happens, for example, with well-studied populations such as Type Ia and Type II SNe, and with rarer populations including Type Ib, Ic, and broad-line Ic (or Ic-BL) SNe (see e.g. Fig. 1 in Whitesides et al. 2017). Such a plot is presented in Fig. 1, where the positions of SN 2021lwz

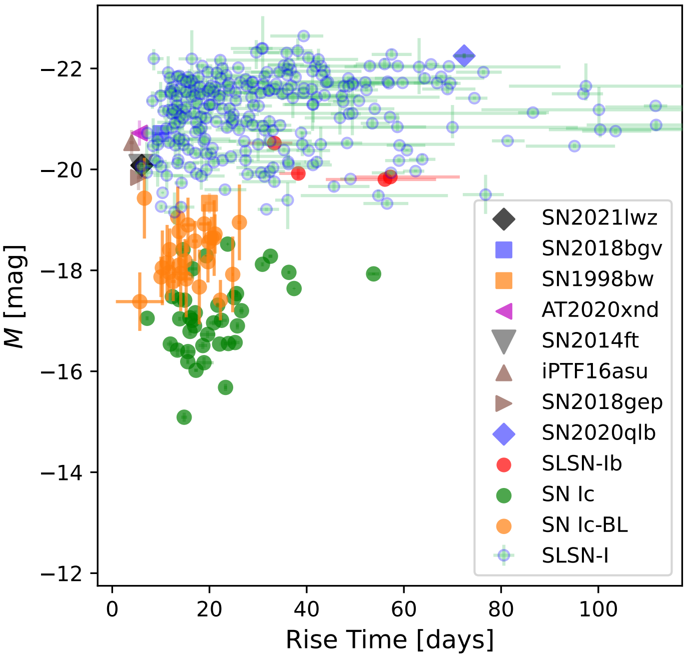

Fig. 1. Rise times, $t_{\rm rise,10\%}$, versus g-band absolute magnitudes, M_g, for SLSNe-I (Gomez et al. 2024), normal SNe Ic (from Barbarino et al. 2021) and SNe Ic-BL (from Taddia et al. 2019). As in Chen et al. (2023a) the M_g of the Sn Ic and SN Ic-BL is computed from the r-band magnitudes using a colour correction of ∼0.36 mag. The rise times of these two populations are measured from the explosion dates in the r band, which are slightly longer than $t_{\rm rise,10\%}$. The data used for the labelled individual sources are from our compilation discussed in Sects. 3.5 and 5.

(see Sect. 3.4) and several other objects of various types are displayed.

The empirical method used to study such new populations of transients, and to try to understand the nature of their progenitors and their environments, is therefore to gather as many data as possible. This includes collecting multi-band, multi-messenger, high-cadence photometry to estimate the full energy budget spatially deployed by the explosion over time (e.g. Prentice et al. 2016; Kornilov et al. 2023). This requires high-cadence spectroscopy in order to study the chemical evolution of the photosphere (e.g. Quimby et al. 2011; Könyves-Tóth 2022; Könyves-Tóth & Seli 2023). When possible, this means acquiring polarimetry data to study the time-evolution of the geometry of the systems closely connected to the explosion (e.g. inner core, jets; see Nagao et al. 2024; Soker 2024) or products resulting from the explosion (e.g. photosphere evolution, ejecta; see Inserra et al. 2016; Leloudas et al. 2017). Obviously, gathering such data is a complex task, and it is even more complex for fast-rising events; moreover, the lack of data obtained on some specific objects often prevents us from achieving the full picture in one collection. Nevertheless, gathering data and increasing the sample on several members of the same class of objects retrospectively helps to better understand the said class. Such progress is made in parallel to theoretical and numerical modelling developments (e.g. Khatami & Kasen 2024; Omand & Jerkstrand 2023), which are crucial to understanding and interpreting the data, and ultimately to put constraints on, or to identify the channel formation of such new or peculiar transients or SNe. In this context of luminous transients, SN 2021lwz is a particularly intriguing object deserving of a dedicated in-depth study.

Located at RA = 09h44mn47.390s, Dec = +34°42′44.21″, SN 2021lwz (also known as ZTF21abaiono, PS21fcj, ATLAS21oii, and Gaia21cvf) was discovered by Fremling (2021) on May 10, 2021 from ZTF[1] public alerts (Patterson et al. 2019). The discovery magnitude obtained with the ZTF-cam mounted on the Palomar 1.2 meter Oschin was of $g = 18.76$ mag (AB system). The transient was classified on May 15, 2021 as an SLSN-I at a redshift $z = 0.065$ by Perley et al. (2021b) from the analysis of a Keck1 Low Resolution Imaging Spectrometer (LRIS, Oke et al. 1995)[2] spectrum. For that reason, SN 2021lwz entered into our sample of H-poor SLSNe for follow-up. Subsequently, though, we realised that some of the pre-peak spectra are not similar to typical H-poor SLSN spectra at similar phases, and we therefore decided to investigate this source in more detail. Indeed, SN 2021lwz is also part of the sample of rare luminous SNe discussed by Gomez et al. (2022). This type of transient appearing to form a continuum between Type Ic SNe and SLSNe is expected to make up ~0.4% of all observed core-collapse SNe (CCSNe; Gomez et al. 2022). Additionally, SN 2021lwz is a fast-rising SLSN ranging in the low absolute magnitude range, as most of the He-rich (He-rich) SLSNe. This type is rare, but a sample of seven he-rich SLSNe was reported by Yan et al. (2020). In this sample, the spectroscopically well-sampled SLSN SN 2019hge (ZTF 19aawfbtg) was shown to be of similar spectral type as PTF 10hgi, the only known He-rich SLSN at the time. Both were used to identify six more He-rich SLSNe, thus increasing the sample of such known events to a total of eight members.

In this paper we present an intensive study of SN 2021lwz. All the data obtained concerning SN 2021lwz and its host galaxy are presented in Sect. 2. The data analysis of SN 2021lwz provided in Sect. 3 is followed by a detailed modelling of the SN and its host galaxy in Sect. 4. In order to better understand and contextualise the nature of SN 2021lwz, comparisons with some SLSNe and other typical SNe and exotic transients are discussed in Sect. 5. Our conclusions are given in Sect. 6.

Throughout this paper, the photometric measurements are reported in the AB system and the uncertainties are provided at 1σ confidence. We used the *Planck* 2018 flat Lambda Cold Dark Matter (Λ−CDM) cosmology model ($\Omega_m = 0.31, H_0 = 67.7$ km/s; Planck Collaboration I 2020).

2. Data

In this section we present data and information about the host galaxy. We also present the photometry, spectroscopy, and polarimetry data obtained at several epochs on SN 2021lwz. Most of these observations were coordinated through the ZTF Fritz–Marshal system (van der Walt et al. 2019; Coughlin et al. 2023). The reference epoch of maximum light is defined as $\mathrm{MJD_{max}} = 59350.9 \pm 1.0$ days with respect to the g band, as from a visual inspection. The extinction contribution from our Galaxy in the line of sight to SN 2021lwz and its host is $A_{\mathrm{MW,u}} = 0.054, A_{\mathrm{MW,g}} = 0.042, A_{\mathrm{MW,r}} = 0.029, A_{\mathrm{MW,i}} = 0.021$ and $A_{\mathrm{MW,z}} = 0.016$ (Schlafly & Finkbeiner 2011).

2.1. Host photometry

The highly accurate spectroscopic redshift $z = 0.065$ of SN 2021lwz was determined from narrow, H-alpha host-galaxy emission and probable [OIII] emission at a redshift consistent with the less accurate redshift obtained with the SNID analysis (Perley et al. 2021b). The host galaxy at RA = 09h44mn47.397s, Dec = +34°42′44.63″ was detected in archival Sloan Digitized Sky Survey (SDSS)[3] and Legacy Survey (LS)[4] images. It can be seen as the blue feature marked by the yellow circle in the LS image plotted in Fig. 2.

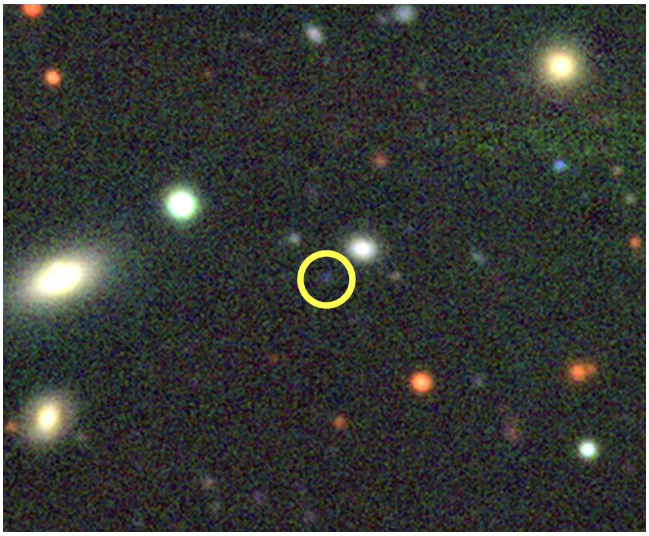

Fig. 2. LS DR 10 image of SN 2021lwz's host, as shown by the faint feature centred in the yellow circle, and its environment. The field of view is of about 120″ by 90″ in size. North is up and east is left in the equatorial frame.

We retrieved science-ready co-added images from the Panoramic Survey Telescope and Rapid Response System (Pan-STARRS, PS1) DR1 (Chambers et al. 2016) and the Sloan Digital Sky Survey Data Release 9 (SDSS DR 9; Ahn et al. 2012). In addition, the field was observed with the 3.58-m Canada France Hawaii Telescope telescope equipped with MegaPrime in the u and r bands between 2016 and 2019. We retrieved the level-2 data from the CADC and combined them using Swarp version 2.38.0 (Bertin 2010) to create a co-added image. We measured the brightness in all images using an aperture photometry tool presented in Schulze et al. (2018) that is based on Source Extractor (Bertin & Arnouts 2010). The measurements in these different bands are given in Table A.1.

One survey observed that part of the sky in the near-infrared (NIR) with the Wide Field Camera (WFCAM) mounted on the United Kingdom Infrared Telescope[5]. The Large Area Scale (LAS) survey footprint of the UKIDSS Data Release 9[6] includes the coordinates position of SN 2021lwz. This survey, whose limit magnitudes are all lower than 20.2 mag in the Y, J, H, and K bands, does not show any detection of the host of SN 2021lwz (see Lawrence et al. 2007). This is in agreement with our results from the modelling of the host (see Sect. 4.4).

2.2. Spectroscopy

In addition to the Keck1 LRIS public spectrum used to classify the transient, we acquired spectra with the Spectral Energy

[1] *Zwicky* Transient Facility: https://www.ztf.caltech.edu
[2] LRIS: https://www2.keck.hawaii.edu/inst/lris/lrishome.html
[3] http://skyserver.sdss.org/dr17/VisualTools/explore/summary
[4] Legacy Survey, https://www.legacysurvey.org/
[5] UKIRT, https://about.ifa.hawaii.edu/ukirt/
[6] https://cdsarc.cds.unistra.fr/viz-bin/cat/II/319

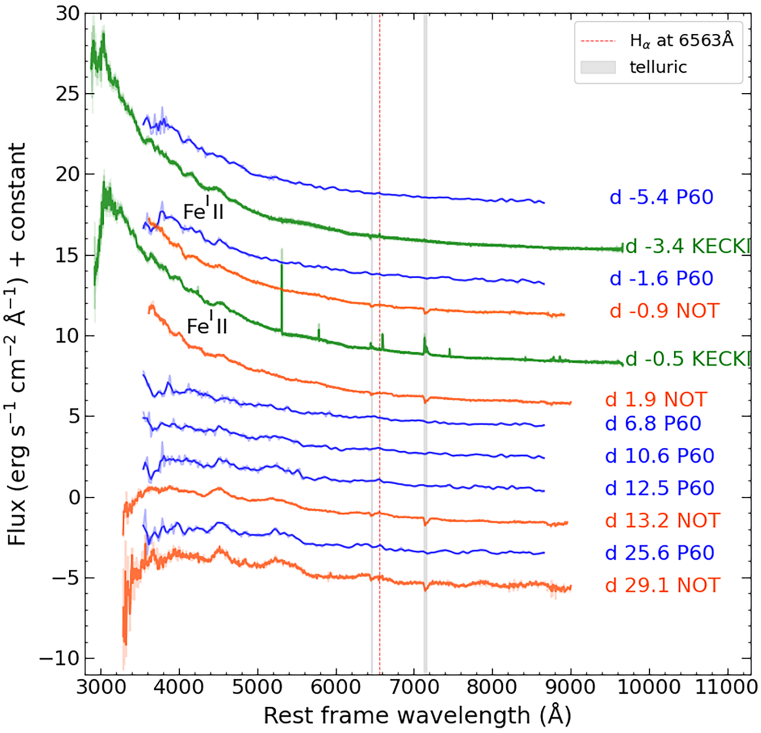

Fig. 3. Spectral sequence of SN 2021lwz. Spectra taken with the P60 are shown in blue, with the NOT in orange, and with the Keck I telescope in green. All the spectra were smoothed using a Savitzky–Golay low pass filter. Un-smoothed data and measurement errors are shown with a lighter shade of the same colour. Each spectrum is marked with its phase in rest frame days relative to maximum g-band flux as well as the telescope used for measurement. The Fe II P-Cygni profile minima used for velocity estimation are marked in dark red. Figure 6 zooms in on the Fe II lines.

Distribution Machine (SEDM; Blagorodnova et al. 2018) on the Palomar Observatory 60 inch telescope (P60), the LRIS on the 10 m Keck I telescope, and the Andalucia Faint Object Spectrograph and Camera (ALFOSC)[7] on the 2.56 m Nordic Optical Telescope (NOT). SEDM spectra were reduced according to Rigault et al. (2019), Kim et al. (2022). The LRIS spectrum was reduced using LPipe as described by Perley (2019). ALFOSC spectra were reduced using PyNOT[8]. A spectrophotometric standard star was used to calibrate each spectrum. A summary of the spectra obtained on SN 2021lwz is given in Table B.1. In Fig. 3 we show the spectral evolution of SN 2021lwz. The spectra were taken between −5.4 rest frame days and +29.1 days relative to the g-band maximum.

The brightness and low-redshift of SN 2021lwz motivated observations in the NIR. One spectrum was obtained at +12.6 days, rest frame, with the Near-Infrared Echellette Spectrometer (NIRES Wilson et al. 2004), a prism cross-dispersed NIR spectrograph mounted on the Keck II telescope. The spectrograph has a power resolution of $R \sim 2700$. It simultaneously covers the $YJHK$ bands over the wavelength range of 0.8–2.4 µm. The spectra were reduced with *spextool* (Cushing et al. 2004) and *Xtellcor* (Vacca et al. 2003) and then combined together. The final spectrum is shown in Fig. 4.

2.3. SN photometry

Photometry of SN 2021lwz was obtained in several filters with the *Swift* satellite (Gehrels et al. 2004), from the ZTF survey (Bellm et al. 2019b), and with the Liverpool Telescope (LT; Steele et al. 2004). Public photometry was retrieved from the ATLAS[9] (Tonry et al. 2018b) public server (as explained in Sect. 2.3.4) Details about the data are given in the following sections. The photometry is shown in Fig. 5. Table C.1 summarises all these measurements.

2.3.1. Swift UVOT data

We observed the field with the 30 cm Ultraviolet/Optical Telescope (UVOT; Roming et al. 2005) aboard the Neil Gehrels Swift Observatory – hereafter *Swift* satellite (Gehrels et al. 2004) – between −2.6 and 20.9 days before and after maximum light (observer frame) in six different filters ($w2$, $m2$, $w1$, u, b, v) from 2086 to 5411 Å. We retrieved the science-ready data from the *Swift* archive[10]. We co-added all sky exposures for a given epoch and filter to boost the S/N using `uvotimsum` in HEAsoft[11] version 6.26.1. Afterwards, we measured the brightness of SN 2021lwz with the *Swift* tool `uvotsource`. The source aperture had a radius of 5″, while that of the background region was significantly larger. The photometry was calibrated with the latest calibration files from September 2020 and converted to the AB system using Breeveld et al. (2011).

2.3.2. ZTF data

Data were acquired with the ZTF that uses the Samuel Oschin 48-inch (1.22 m) Schmidt telescope at Palomar Observatory on Mount Palomar (USA). It is equipped with a 47-square-degree camera (Dekany et al. 2020) and monitors the entire northern hemisphere every 2–3 days in the g and r bands to

[7] http://www.not.iac.es/instruments/alfosc/
[8] https://github.com/jkrogager/PyNOT
[9] https://atlas.fallingstar.com
[10] https://www.swift.ac.uk/swift_portal
[11] https://heasarc.gsfc.nasa.gov/docs/software/heasoft/

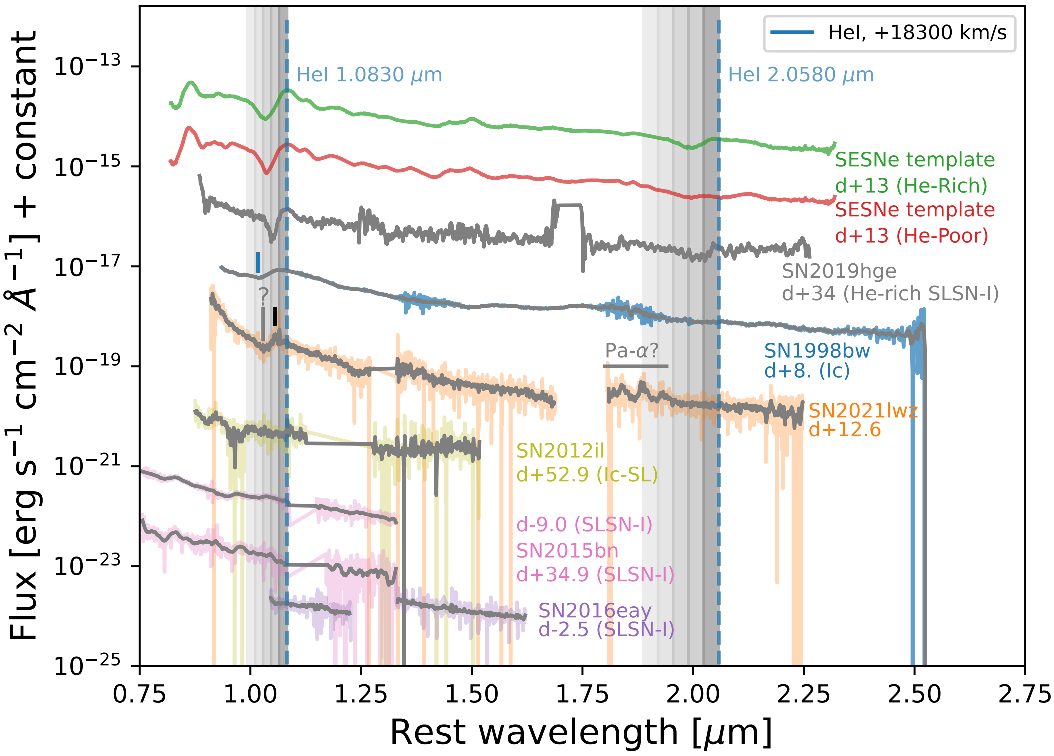

Fig. 4. NIR spectrum of SN 2021lwz obtained with NIRES on Keck II. Also shown are the SESNe template spectra of He-rich (green) and He-poor at phase +13 days produced by Shahbandeh et al. (2022). The NIR spectra of the He-rich SLSN-I SN 2019hge at phase +34 days (grey, smoothed, Yan et al. 2020), of the peculiar and bright Type Ic SN 1998bw at phase +8 days (blue, Patat et al. 2001), of Ic-SL SN 2012il at phase +52.9 days (Inserra et al. 2013), of H-poor SLSN SN 2015bn at phases −9.0 days and +34.9 days (Nicholl et al. 2016a), and of SN 2016eay (or Gaia16apd) at phase −2.5 days (Yan et al. 2017) are also shown for comparison. The observed spectra smoothed using Savitzky–Golay low pass filters are shown in grey. The vertical grey bands show velocity line ranges in bins of 5000 km/s.

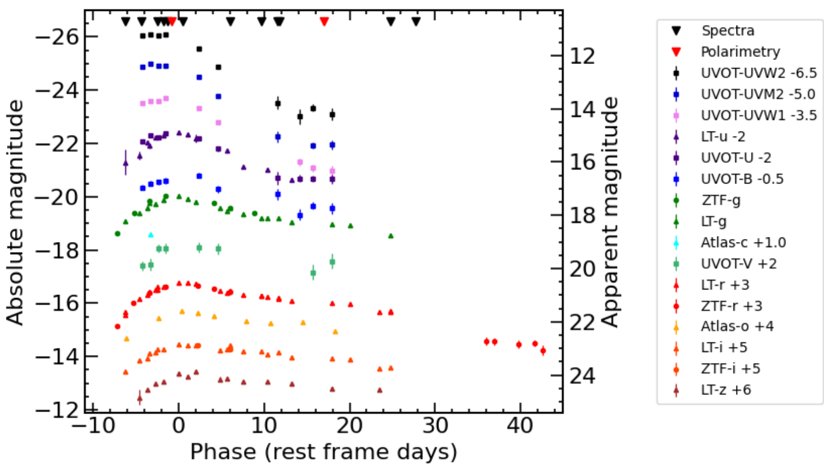

Fig. 5. Absolute-magnitude (rest frame) light curves (see Sect. 3.4 for details) from the ATLAS and Liverpool Telescope SDSS filters as triangles, the *Swift* UVOT filters as squares, and the ZTF filters as circles. The phases of available spectra are shown as black triangles at the top along with the phases of the polarimetry shown as red triangles. Phase = 0 is at peak ZTF *g*-band flux. The light curves were shifted by the indicated amounts for illustration purposes.

a depth of ~20.7 mag (5σ; Bellm et al. 2019b; Graham et al. 2019) as part of the public ZTF Northern Sky Survey (Bellm et al. 2019a). We retrieved the host-subtracted photometry via the ZTF forced-photometry service (Masci et al. 2023) hosted by the NASA/IPAC Infrared Science Archive (IRSA) at IPAC.

2.3.3. Liverpool Telescope data

Observations were taken with the IO:O optical imager on the LT in the Sloan Digital Sky Survey (SDSS) *u*, *g*, *r*, *i*, and *z* filters. Reduced images were downloaded from the LT archive and processed with custom image-subtraction and analysis software (K. Hinds and K. Taggart et al., in prep.). Image stacking and alignment was performed using SWarp (Bertin et al. 2002) where required. Image subtraction was performed using a pre-explosion reference image in the appropriate filter from the Panoramic Survey Telescope and Rapid Response System 1 (Pan-STARRS1) or SDSS. The photometry was measured using PSF fitting methodology relative to Pan-STARRS1 or SDSS standards and is based on techniques from Fremling et al. (2016).

2.3.4. ATLAS data

ATLAS forced photometry data were retrieved from the ATLAS public server[12] (Tonry et al. 2018b; Smith et al. 2020; Shingles et al. 2021). They were clipped and binned to one day using the publicly available code plot_atlas_fp.py[13].

2.4. SN polarimetry

The observation log of the imaging polarimetry obtained with ALFOSC on the Nordic Optical Telescope (NOT) is given in Table D.1. Linear rest frame polarimetry was obtained at +1.0 and +19.0 days. The polarimetry was obtained using a half-wave plate (HWP) in the FAPOL unit and a calcite plate mounted in the aperture wheel. The calcite plate provides the simultaneous measurement of the ordinary and the extraordinary components of two orthogonal polarised beams (see Fig. D.1). The HWP can be rotated in steps of 22.5° from 0° to 337.5°. As a standard, we used four angle positions (0°, 22.5°, 45°, and 67.5°) to sample the Stokes parameter space. The photometry of the ordinary and extraordinary beams was done using aperture photometry with size ∼2–3 times the full width at half maximum (FWHM) of point sources in the images. For multiple sequences of four HWP angles the polarisation is obtained by summing up the fluxes from the ordinary and extraordinary beams to minimise uncertainty propagation.

3. Data analysis

In this section we derive physical parameters associated with the explosion using an analytical approach.

3.1. Spectral analysis using template fitting

In order to obtain a first understanding of the spectral evolution of SN 2021lwz, we ran all the optical spectra through the SuperNova IDentifier (SNID; Blondin & Tonry 2007 and references therein). We first performed a general classification by running the code over our upgraded template database, which, in addition to the standard types (Ia, Ib, Ic, and II) and their subtypes, contains SLSN-I and SLSN-II templates including those of PTF 10hgi (19 spectra with epochs lying between −30 and +312 days with respect to peak in the SN rest frame) and SN 2019hge (2 spectra at epochs 0 and +48 days, respectively); these were used as He-rich SLSN-I templates in Yan et al. (2020, see our Sect. 1).

The analysis provided by SNID shows that none of the spectra of SN 2021lwz obtained before peak (see Table B.1 and Fig. 3) can be matched properly without decreasing some of the values of the default SNID parameters aimed to ensure a statistically robust diagnostic. Fit attempts using only He-rich SLSNe PTF 10hgi or SN 2019hge templates were conducted on the pre-peak spectra without producing any good match. Using the full database, a relatively poor fit is obtained on the −3.4 days Keck spectrum with the Type Ic-SL (Ic-superluminous) PTF10cwr, whose absorption features are smooth compared to those of other SL templates. At maximum light the Keck spectrum at −0.5 days shows similarities with the fast-evolving transient SN 2018bgv. These fits are shown in Fig. E.1. Accurate fits of the ALFOSC spectra of SN 2021wz obtained post-peak are obtained without degrading the default SNID parameters. They suggest that the photosphere of SN 2021lwz evolved as a Ic-BL-like type, in agreement with the first statement provided in the TNS classification report.

At early times, when inspecting by eye it appears that the spectra could be consistent with SLSNe, but with higher velocities than we are used to seeing. This could explain why the fits with SLSNe favour lower redshifts. This may also happen because SNID tries to adjust the W-feature often attributed to O II, but it is known that different lines of other elements such as Fe II are expected in this wavelength range. This will be discussed further in our analysis. The fits obtained with SLSN-I SN 2016wi and with the Type Ic-SL SN LSQ12dlf, shown in Fig. E.1, middle, point to more accurate redshift consistency. Using a slightly lower value of four for the *rlap* factor, it is possible to produce lower quality fits with late-time spectra of the peculiar Type Ic SN 1998bw (bottom) whose NIR spectral properties are discussed and compared with those of the SN 2021lwz NIR spectrum in Sect. 3.2.

3.2. NIRES spectrum

The NIR spectrum of SN 2021lwz, obtained at +12.6 days in the rest frame and after the peak, is shown in Fig. 4. It provides valuable information for comparison with several types of SNe observed in the NIR. The spectrum is smooth and relatively featureless with an absorption feature centred at ∼1.0290 µm (see the grey vertical line with an exclamation mark). If that feature was to be produced by He I, 1.0830 µm, its velocity would be ∼16 200 km s^{-1}, i.e. of about the same order as the ejecta velocity derived a few days before maximum light, and about two times larger than the photosphere velocities at the late phase (∼7500 km s^{-1}), as derived from the optical-spectra analysis discussed in the following sections. At this late-phase velocity, any He I, 1.0830 µm absorption feature would be encountered at a wavelength position centred close to 1.0559 µm as indicated by the vertical black line. For comparison, the high-velocity 18 000 km s^{-1}, He I, 1.0830 µm absorption feature possibly detected in the peculiar Type Ic SN 1998bw (Patat et al. 2001) is shown by the vertical blue line. Similar comparisons can be done with the He-rich and He-poor template spectra at phase +13 days (d+13) of stripped-envelope SNe (SESNe) derived from a principal component analysis of Types IIb, Ib, Ic, and Ic-BL by Shahbandeh et al. (2022), and with the +34 days He-rich spectrum of SLSN-I SN 2019hge (Yan et al. 2020). At higher wavelengths, these three spectra show spectral features that are not seen in the spectrum of SN 2021lwz, whose smooth features look more similar to those seen in the spectrum of SN 1998bw.

Additional unidentified absorption or emission features are seen in the spectrum of SN 2021lwz in the wavelength range ∼1.800−1.950 µm, which are not seen in the SESNe template spectra. In this wavelength range, some features are seen in the spectra of SN 2008ax and SN 1998bw in sky-line-contaminated regions of the spectra making any direct comparison difficult. At higher wavelength, the SN 2021lwz spectrum does not show any hint of an absorption feature that could be produced by He I, 2.0580 µm.

To assess if SN 2021lwz could be a Type I SLSN, we also made comparisons with spectra of SN 2015bn at phases of −9 days and +34 days (Nicholl et al. 2016b), of Gaia16apd at phase −2.5 days (Yan et al. 2017, and references therein), and of SN 2012il at phase +52.9 days. None

[12] https://fallingstar-data.com/forcedphot/
[13] https://gist.github.com/thespacedoctor/86777fa5a9567b7939e8d84fd8cf6a76

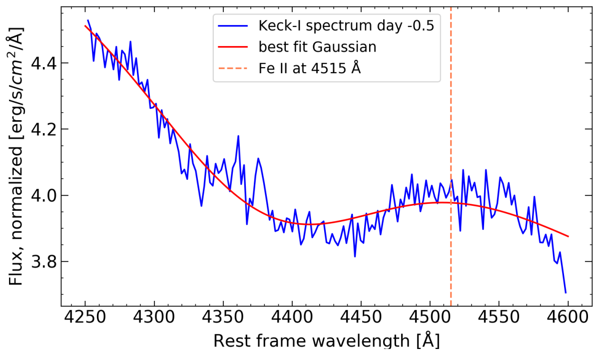

Fig. 6. SN 2021lwz P-Cygni profile for Fe II at 4515 Å from the Keck I spectrum at −0.5 rest frame days.

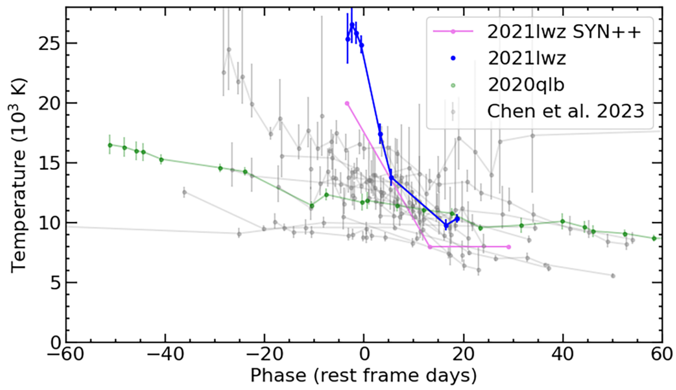

Fig. 7. SN 2021lwz temperature evolution compared to SN 2020qlb (West et al. 2023); data from Table 1 and 31 SLSNe-I from Chen et al. (2023a).

of these spectra are at a phase similar to the NIR spectrum of SN 2021lwz, and the wavelength coverage is sometimes limited, preventing us from making meaningful comparisons; however, all in all, they look different from the spectrum of SN 2021lwz.

3.3. P-Cygni velocity estimation

We used the Fritz data science platform to cycle through all of the available lines and find that Fe II is the best one that matches the broad feature near 4515 Å seen in some of the spectra at a redshift of $z = 0.065$. In this respect, we mainly attributed the prominent P-Cygni-like profiles in the Keck I spectra at −3.4 and −0.5 days to Fe II at 4515 Å. They are marked in black in Fig. 3. We estimated the ejecta velocity according to the longitudinal relativistic Doppler shift. We used the `scipy.optimize.curve_fit` algorithm to fit an equation consisting of a straight line component to match the continuum, and a Gaussian component to match the absorption feature to P-Cygni profile data as shown in Fig. 6. The resulting covariance matrices and the corresponding parameter fit values of $\lambda_{\min} = 4293.8$ Å and $\lambda_{\min} = 4379.5$ Å were then used to estimate the absorption-line velocity of $15040 \pm 570\,\mathrm{km\,s^{-1}}$ at −3.4 days and $9130 \pm 350\,\mathrm{km\,s^{-1}}$ at −0.5 days, respectively.

3.4. Light curve analysis

The absolute magnitude was calculated as

$$\mathrm{M} = \mathrm{m} - \mu - K_{\mathrm{corr}} - \mathrm{A_{MW}} - \mathrm{A_{host}}, \quad (1)$$

where μ represents the distance modulus (which is equal to 37.40 for a redshift of 0.065); K_{corr} is the correction factor for the difference in filter bandpass between the observer and the rest frame; $\mathrm{A_{MW}}$ is the extinction caused by the Milky Way; and $\mathrm{A_{host}}$ is the extinction caused by the host galaxy.

We only used the first term of the K-correction as described by Hogg et al. (2002), as shown here:

$$K_{\mathrm{corr}} = -2.5 \times \log_{10}(1 + z) = -0.07\,\mathrm{mag}. \quad (2)$$

The Fitzpatrick (1999) extinction model was used to calculate the MW dust extinction based on the parameters $R_V = 3.1$ and $E(B - V) = 0.013$ mag. We assumed that the extinction from the host galaxy is negligible since no absorption lines – for example, Na I Doublet absorption lines – are visible. The resulting absolute-magnitude (rest frame) light curves from LT, UVOT, ATLAS, and ZTF are plotted in Fig. 5.

The rising rate is calculated using the g-band data. At −7.1 days the g-band absolute magnitude is −18.7 mags. At zero days the g-band absolute magnitude is −17.2 mags. The delta mag on the rise close to the peak is therefore 1.5 mags/7.1 days = 0.2 mags per day.

3.5. Photospheric radius and temperature evolution

We estimated the photospheric temperature and radius evolution at the phases where full sets of UVOT measurements are available and interpolated ZTF, LT, and ATLAS-o light curve-measurements using Gaussian process (GP) regression, which utilises the Python package `GEORGE` (Ambikasaran et al. 2015) with a Matern 3/2 kernel. We then used the `scipy.optimize.minimize`[14] algorithm to fit a Planck function (blackbody) to the datasets.

We find that the three UVOT UV filters are consistently incompatible with the best-fit blackbody. We attribute the problem to line blanketing, as seen in other SLSNe (see e.g. Yan et al. 2017). We therefore excluded the three UV filter measurements from UVOT before rerunning the blackbody fits to create the photospheric temperature and radius evolutions. The temperature evolution and the radius evolution of SN 2021lwz are compared to a sample including those of SN 2020qlb (West et al. 2023) and those of the 31 SLSNe-I provided in the online version of Table A6 of Chen et al. (2023a) in Figs. 7 and 8, respectively.

3.6. Ejecta-velocity estimation

The time derivative of the best-fit polynomial of the SN 2021lwz radius evolution gives rough estimates of the photospheric velocity at relevant phases. At epochs just after explosion the photospheric velocity should approximate the ejecta velocity. At later epochs, P-Cygni absorption-line features estimate velocities outside the photosphere. In Fig. 9 we compare the photospheric velocity evolution to the P-Cygni velocity estimate from Sect. 3.3.

3.7. Bolometric light curve estimation

At the eight epochs where UVOT data are available we calculated the spectral luminosity (L_λ) for each UVOT filter mea-

[14] https://docs.scipy.org/doc/scipy/reference/generated/scipy.optimize.minimize.html

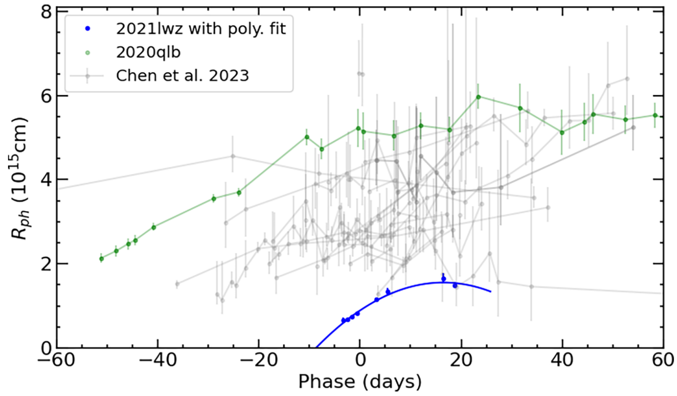

Fig. 8. SN 2021lwz radius evolution compared to SN 2020qlb (West et al. 2023) and to 31 SLSNe-I from Chen et al. (2023a). A best-fit second-degree polynomial is also plotted for SN 2021lwz.

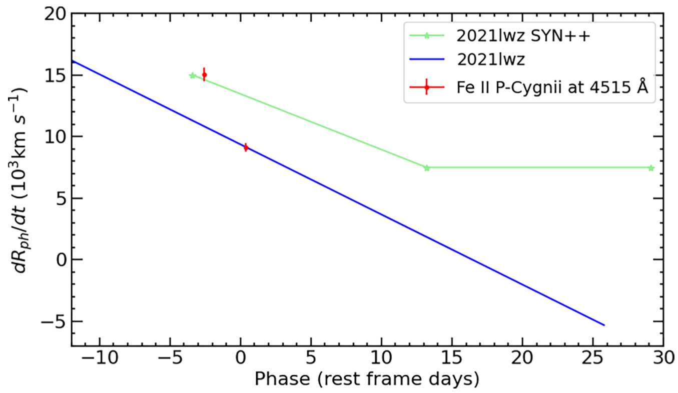

Fig. 9. SN 2021lwz photosphere velocity estimates from the time derivative of the best-fit polynomial to the radius evolution of SN 2021lwz shown in Fig. 8; P-Cygni velocity estimates from the Keck I spectra at −3.4 and −0.5 days; SYN++ data are from Table 1.

surement and GP interpolated filter value from the other filters. Short of the lowest filter value, we created L_λ estimates based on the best-fit blackbody to the UVOT-UV, UVOT-U, and LT-u filter measurements. Long of the highest filter value we created L_λ estimates based on the best-fit blackbody to the optical filter measurements. These extrapolation methods are also used in `SuperBol` software (Nicholl 2018). We then integrated over all wavelengths to create bolometric luminosity estimates at each of the eight epochs, which form the bolometric light curve. These results are shown, modelled, and discussed in Sect. 4.2.

3.8. Photosphere geometry

The polarisation degrees measured on the unpolarised star, BD+52913; on the polarised calibration star, HD 127769; on the field star, STAR 1 (shown in Fig. D.1); and on SN 2021lwz are all displayed in Table D.2. The instrumental polarisation (IP) degree is of the order of 0.1% at each epoch. This component, which is retrieved in the parameter space of the Stokes Q and U parameters, is removed from the components of the other sources (IP correction). We used the polarised star HD 127769 to calculate the zero polarisation angle (ZPA), which is used to rotate the Stokes Q, U parameters from the ALFOSC FAPOL instrument reference frame to the sky reference frame in equatorial coordinates. The polarisation angles are counted positively from north to east. We used the polarimetry available on STAR 1 in

Table 1. SYN++ modelling of SN 2021lwz.

Date	MJD	Phase (days)	$T_{\rm phot}$ (K)	$v_{\rm phot}$ (km s^{-1})
2021-05-13	59 347	−3.4	20 000	15 000
2021-05-30	59 364	13.2	8000	7500
2021-06-16	59 381	29.1	8000	7500

the field of view of FAPOL (see Fig. D.1) to obtain an estimate of the polarised component of the Galaxy in the vicinity of SN 2021lwz. These estimates are of the same order as their uncertainties, suggesting a low level of the interstellar polarisation (ISP) in this region of the sky. This result is consistent with the polarisation degrees of the two stars HD 82885 ($P = 0.05 \pm 0.12$) and HD 82635 ($P = 0.03 \pm 0.12$) retrieved from the Heiles (2000) agglomeration catalog. These two stars are at distances lower than two degrees on the plane of sky from the central coordinate position of SN 2021lwz. The levels of polarisation obtained on SN 2021lwz after ISP correction using STAR 1 Stoke Q and U parameters are displayed in the last column of Table D.2. The final values are obtained after bias correction following the equation given in Wang et al. (1997):

$$P = (P_{\rm obs} - \sigma_P^2/P_{\rm obs}) \times h(P_{\rm obs} - \sigma_P), \quad (3)$$

where h is the Heaviside function, $P_{\rm obs}$ is the observed polarisation, and σ_P is the 1σ error. The final measurements – $p_{\rm db} = 0.00 \pm 0.14\%$ at +1 day (rest frame), and $p_{\rm db} = 0.25 \pm 0.18\%$ at +19 days (rest frame) – are consistent with null-polarisation. They suggest that the geometry of the photosphere of SN 2021lwz, which is almost spherical (from our observer point of view) did not change with time. Similarly, there is no hint that the SN's photosphere interacted with the CSM.

4. Data modelling

4.1. Optical spectrum evolution and chemical composition

To study the spectroscopic evolution of SN 2021lwz, we modelled the available photospheric phase spectra utilising the SYN++ code (Thomas et al. 2011). This makes it possible to fit some global parameters that refer to the overall model spectrum, such as the temperature ($T_{\rm phot}$) and the velocity ($v_{\rm phot}$) at the photosphere. The lines of the individual ions can be fitted via local parameters, such as code the optical depth (τ), the velocity width of the line forming region ($v_{\rm min}$ and $v_{\rm max}$), the scale height parameter of the optical depth above the photosphere (aux), and the excitation temperature ($T_{\rm exc}$), assuming local thermodynamic equilibrium.

For SN 2021lwz, we have spectra available at 12 different epochs from −5.4 days to +29.1 days, rest frame, relative to the moment of the maximum light. Table 1 presents the date of observation of the modelled high-resolution spectra together with their phases, and the $T_{\rm phot}$ and $v_{\rm phot}$ values of their best-fit models obtained using SYN++. The possibilities, constraints, and uncertainties of the usage of SYN++ and its parameters are discussed in detail in Könyves-Tóth (2022).

Figure 10 shows the spectrum modelling of SN 2021lwz. In the top panel, the modelling of the −3.4 d phase spectrum of SN 2021lwz can be seen. The best-fit $T_{\rm phot}$ and $v_{\rm phot}$ values are in Table 1. The identified elements are C II, O I, Na I, Mg II, Si II, Ca II, Ti II, and Fe II. Regarding this, SN 2021lwz is more similar to a normal Type Ic SN than an SLSN. The pre-maximum spectrum of ~2/3 of the SLSNe-I usually contains a W-shaped absorption blend between ~4000 and 5000 Å, while the remaining ~1/3 of the SLSNe-I show similar features to SN 2015bn (see Könyves-Tóth 2022). However, the −3.4 d phase spectrum of SN 2021lwz does not show resemblance to any of these SLSN-I sub-types.

The bottom panel of Fig. 10 shows the modelling of the +13.2 d and the +29.1 d phase spectra, which are quite similar to each other. By these phases, both the photospheric velocity and temperature decreased significantly ($T_{\rm phot}$ = 8000 K and $v_{\rm phot}$ = 7500 K), and besides Fe II, Ca II, Si II, Mg II, O I, and C II, He I was included in the best-fit model.

In Table F.1, the best-fit local parameter values obtained in SYN++ are collected. The SYN++ modelling analysis suggests SN 2021lwz is a intermediate Type Ic/Ic-BL transient rather than an SLSN-I.

To conclude, we point out that any difference between $T_{\rm exc}$ and $T_{\rm phot}$ can be explained by the presence of non-local thermodynamic equilibrium (NLTE) effects. In the case of LTE, $T_{\rm exc} = T_{\rm phot}$ for each ion; however, in SNe, NLTE effects usually play a role in the spectrum formation. Although SYN++ is not an NLTE code, such as TARDIS (Kerzendorf & Sim 2014), which can appropriately take into account every difference from LTE, choosing a $T_{\rm exc} \neq T_{\rm phot}$ indicates that there is some divergence from the LTE. If we change the $T_{\rm exc}$ of a given ion in SYN++, the line ratios and strengths become different. We chose the best-fit model accordingly.

4.2. Bolometric light curve modelling

We compared semi-analytic models to the bolometric light curve to determine the most probable power source of the SN. The radioactive source and magnetar source models used by West et al. (2023, described in Sect. 7) (Arnett 1982; Kasen & Bildsten 2010; Woosley 2010), were employed using the ejecta velocity estimate from Sect. 3.6. Our main conclusion is that the light curve cannot be fitted with $M_{ni} \leq M_{ej}$. The details of this analysis are given in Appendix G.

There are no signs of narrow lines in the spectra indicating interaction, but shock breakout from interaction with extended material (Nakar & Sari 2010; Nakar & Piro 2014; Piro 2015) has been used to explain the light curve of the similar transient SN 2018gep (Ho et al. 2019; Pritchard et al. 2021). We did not explicitly use this model, but we note that similar parameters ($M_{\rm ej}$ = 8 $M_\odot$, $E_{\rm ej}$ = 2 × 10^{52} erg, $M_{\rm CSM}$ = 0.02 $M_\odot$, and $R_{\rm CSM}$ = 3 × 10^{14} cm; Ho et al. 2019) could likely also reproduce the light curve of SN 2021lwz.

4.3. Multi-band light curve modelling

We performed inference on the multi-band photometry using the REDBACK (Sarin et al. 2024) magnetar-driven SN model including ejecta acceleration and non-vacuum dipole spin-down (Omand & Sarin 2024). We used the PYMULTINEST sampler (Buchner et al. 2014) implemented in BILBY (Ashton et al. 2019; Romero-Shaw et al. 2020) and sampled in flux density with a Gaussian likelihood. The uncertainty presented is only the statistical uncertainty in the fits, and it does not include systematic uncertainty inherent to the simplified one-zone REDBACK model.

We sampled the explosion time with a uniform prior of up to 100 days before the first observation; an extinction term, A_V, with a uniform prior between zero and two; and a white-noise

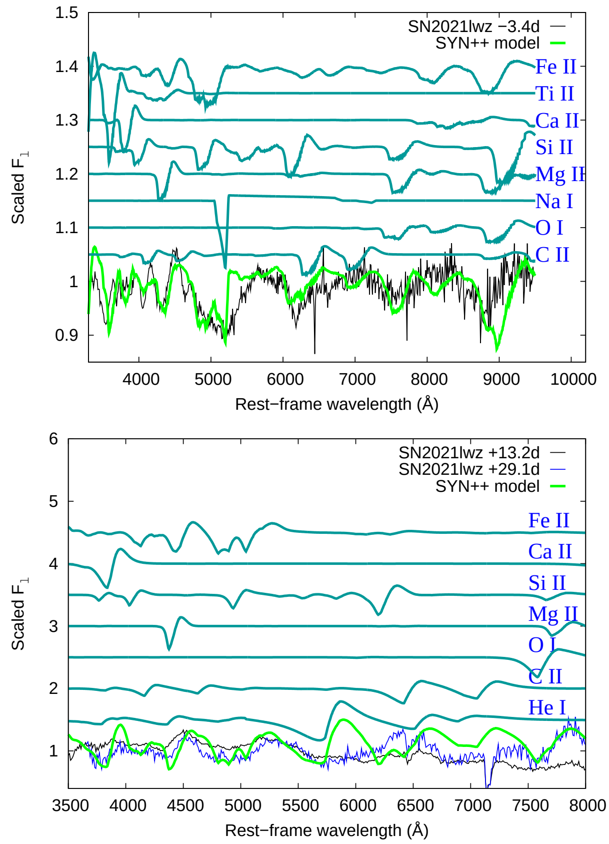

Fig. 10. Best-fit SYN++ models of the spectra of SN 2021lwz. Top: Modelling of the −3.4 d phase spectrum. Bottom: Best-fit model applied to the +13.2 d and the +29.1 d phase spectrum. All spectra were corrected for interstellar reddening ($E(B-V)$ = 0.0108) and redshift. The spectra were continuum normalised using the Planck curve fitted previously using SYN++ before plotting. Green represents the best-fit model, while vertically shifted blue lines represent the single-ion contributions to the overall model spectra.

term. We constrained the total rotational energy of the magnetar to be $E_{\rm rot} \lesssim 10^{53}$ erg. We fixed the photospheric plateau temperature to a value of 8000 K to be consistent with the value found in Sect. 4.1. The physical parameters and priors used are listed in Table 2. Uniform priors are denoted by U, and log-uniform priors are denoted by L.

The fitted light curve is shown in Fig. 11, and the posterior for the parameters is in Fig. H.1. The model fits the peak of the light curve well in all bands, but underestimates the flux in the UV bands from around 14 days post-peak. We find an initial luminosity of $L_0 \approx 3 \times 10^{45}$ erg s^{-1}, spin-down timescale of $t_{\rm SD} \approx$ one day, and an ejecta mass of $M_{\rm ej} \approx 0.24\, M_\odot$. These values are similar to that of the luminous fast-blue optical transient (LFBOT) AT 2020xnd (i.e. the ZTF source ZTF20acigmel; see e.g. Perley et al. 2021a), the USSN SN 2014ft (see Table 2 in Omand & Sarin 2024), and iPTF16asu (see Table 2; and Whitesides et al. 2017; Wang et al. 2019; Wang & Gan 2022), including a similar higher magnetar rotational energy of ~4 × 10^{50} erg, but a lower explosion energy of ~2 × 10^{49} erg. We find the braking index, n, to be ~4.5, and we rule out a vacuum dipole (n = 3) with >95% confidence; this is similar to the cases of SN 2015bn and SN 2007ru (Omand & Sarin 2024).

The distribution of ejecta velocities, peak photospheric temperatures, and several timescales is shown in Fig. 12. The final ejecta scale velocity is around 11 000 km s^{-1}, which is lower than

Table 2. Best-fit parameters for the magnetar model obtained on SN 2021lwz.

Parameter Symbol	Definition	Prior	Best Fit Value SN 2021lwz	Best Fit Value iPTF16asu	Units Units
$\log(L_0)$	Initial Spin-Down Luminosity	L[40.0,50.0]	$45.42^{+0.28}_{-0.26}$	$45.45^{+0.74}_{-0.45}$	erg s^{-1}
$\log(t_{\rm SD})$	Spin-Down Timescale	L[2.0,8.0]	$4.91^{+0.29}_{-0.28}$	$4.64^{+0.37}_{-0.61}$	s
n	Magnetar Braking Index	U[1.5,10]	$4.56^{+0.80}_{-0.74}$	$8.41^{+1.15}_{-1.75}$	
$M_{\rm ej}$	Ejecta Mass	L[0.1,100]	$0.24^{+0.04}_{-0.04}$	$0.17^{+0.03}_{-0.03}$	$M_\odot$
$E_{\rm SN}$	Supernova Explosion Energy	L[0.01,2]	$0.02^{+0.02}_{-0.01}$	$0.59^{+0.15}_{-0.07}$	10^{51} erg
κ	Ejecta Opacity	U[0.05,0.20]	$0.06^{+0.01}_{-0.00}$	$0.06^{+0.01}_{-0.01}$	cm^2 g^{-1}
$\log(\kappa_\gamma)$	Ejecta Gamma-Ray Opacity	L[-4,4]	$1.65^{+1.54}_{-1.62}$	$0.27^{+0.22}_{-0.16}$	cm^2 g^{-1}

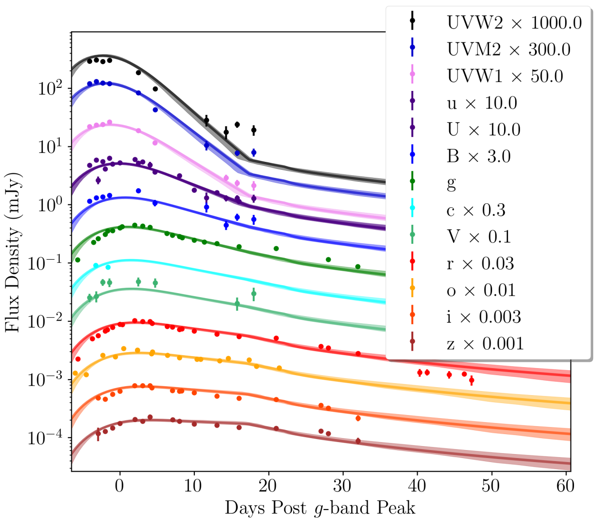

Fig. 11. Fitted multi-band light curve for SN 2021lwz. The solid lines indicate the light curve from the model with the highest likelihood in each band, while the shaded area indicates the 90% credible interval.

the inferred photospheric velocity of 15 000 km s^{-1}; this implies that most of the material is travelling at much lower velocity than the photosphere at early times, although by the peak the photosphere has receded into the bulk of the material. The photospheric temperature at the peak is around 24 000 K, which is slightly higher than the best-fit model temperature of 20 000 K inferred by the spectral analysis, although not significantly higher. The diffusion time of the SN,

$$t_{\rm diff} \approx \sqrt{\frac{3\kappa M_{\rm ej}}{4\pi c v_{\rm ej}}}, \quad (4)$$

$$\approx 14.5\,{\rm days}\left(\frac{\kappa}{0.1\,{\rm cm^2\,g^{-1}}}\right)^{0.5}\left(\frac{M_{\rm ej}}{M_\odot}\right)^{0.5}\left(\frac{v_{\rm ej}}{10\,000\,{\rm km\,s^{-1}}}\right)^{-0.5}, \quad (5)$$

is very short (only ∼5 days) due to the low ejecta mass. The bolometric peak timescale is inferred to be ∼7 days, and the g-band peak timescale is ∼10 days; the discrepancy between these values is consistent with the high photospheric temperature and rapid cooling around the peak. From the intrinsic bolometric luminosity we derive $T_{\rm rise,10\%} = 6.1 \pm 0.3$ days, and $T_{{\rm rise},e} = 4.9 \pm 0.3$ days for the rest frame. The SN is expected

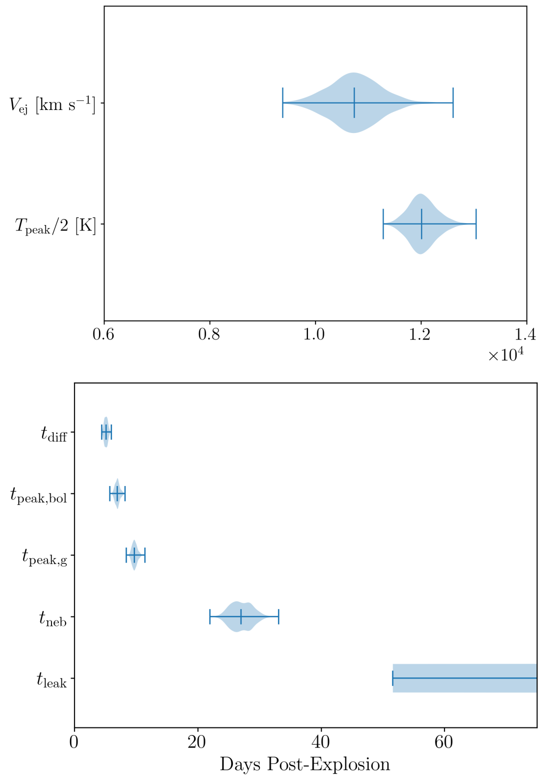

Fig. 12. One-dimensional posteriors of various quantities calculated by the light curve fit. The median values are indicated by the vertical blue lines within the distribution. *Top*: The inferred scale velocity of the ejecta and the temperature of the photospheric at bolometric peak, divided by two to place them on the same scale. *Bottom*: The diffusion timescale, gamma-ray leakage timescale, bolometric-peak timescale, g-band-peak timescale, and nebular timescale.

to enter the nebular phase on a timescale of (Nicholl et al. 2017)

$$t_{\rm neb} \approx \sqrt{\frac{3\kappa M_{\rm ej}}{4\pi v_{\rm ej}^2}}, \quad (6)$$

$$\approx 80\,{\rm days}\left(\frac{\kappa}{0.1\,{\rm cm^2\,g^{-1}}}\right)^{0.5}\left(\frac{M_{\rm ej}}{M_\odot}\right)^{0.5}\left(\frac{v_{\rm ej}}{10\,000\,{\rm km\,s^{-1}}}\right)^{-1}, \quad (7)$$

which is ∼27 days post-explosion, or only ∼17 days post-g-band peak. This could imply that the final two observed spectra, at +26 d and +29 d, were taken during the early nebular phase, even though the spectrum shows no strong evolution between +8 and +29 days. This could also account for the discrepancy between the model and observed photometric points in the late phase. However, it seems more likely that this simplistic estimate of the nebular timescale is not accurate in this situation, which could be because of small-scale asymmetries or the density profile of the ejecta. Since Eqs. (4)–(9) were all derived using a uniform density profile, they could all underestimate the different timescales if the ejecta has a steeper profile (e.g. Suzuki & Maeda 2017). Due to the large inferred gamma-ray opacity, the gamma-ray leakage timescale (Wang et al. 2015),

$$t_{\rm leak} \approx \sqrt{\frac{3\kappa_\gamma M_{\rm ej}}{4\pi v_{\rm ej}^2}}, \tag{8}$$

$$\approx 80\,{\rm days}\left(\frac{\kappa_\gamma}{0.1\,{\rm cm^2\,g^{-1}}}\right)^{0.5}\left(\frac{M_{\rm ej}}{M_\odot}\right)^{0.5}\left(\frac{v_{\rm ej}}{10\,000\,{\rm km\,s^{-1}}}\right)^{-1}, \tag{9}$$

is also very long, with a lower limit of ~50 days. This means that a significant amount of non-thermal emission likely does not escape from the SN during the timescale that we observed. The inferred lower limit on the gamma-ray opacity is ~0.2 cm^2 g^{-1}, which is higher than the mean value of $0.06^{+0.07}_{0.05}$ cm^2 g^{-1} for SLSNe-I (Gomez et al. 2024), although not a significant outlier. The high gamma-ray opacity here may be inconsistent with a pulsar wind nebula (PWN) with low magnetisation (Vurm & Metzger 2021), which would cause the non-thermal emission to be Comptonised and mostly emitted as hard x-rays and gamma-rays. The likely source of opacity for the PWN is photoelectric absorption, which dominates in the soft x-ray regime (see Fig. 4 from Vurm & Metzger 2021). This means that the PWN is likely synchrotron-dominated and may be a strong radio source on longer timescales (e.g. Omand et al. 2018, 2025a).

These parameters differ significantly from those of Gomez et al. (2022) and Gomez et al. (2024), which used the Modular Open Source Fitter for Transients code (`MOSFiT`; Guillochon et al. 2018) to fit several luminous SNe and SLSNe, including SN 2021lwz, using a pure magnetar and magnetar + nickel model, respectively. Gomez et al. (2022) infers a higher ejecta mass of 0.4 $M_\odot$ and a much lower photospheric velocity of ~3000 km s^{-1}. Gomez et al. (2024) infers much higher ejecta and ^{56}Ni masses of ~3 M⊙ and ~0.8 M⊙, respectively, while inferring a much less luminous pulsar of ~10^{40} erg s^{-1}; this means that the luminosity of the SN is mostly powered by ^{56}Ni in that scenario, in contrast to what we find in Sect. 4.2. While the values from Gomez et al. (2022) give a similar diffusion time to our inferred parameters, there is a strong tension between their derived photospheric velocity and the value we inferred from the spectrum. They inferred a lower value of 2×10^{44} erg s^{-1} for the initial pulsar luminosity, but a spin-down timescale of ~15 days. The difference in spin-down timescale, as well as their assumption of vacuum-dipole spin down, means the magnetar rotational energy is similar to our inferred parameters. Any discrepancies likely result from the assumption of constant velocity and decoupling of the magnetar spin-down and ejecta dynamics in the MOSFIT model, which has been shown via radiation hydrodynamics simulations to be unjustified for high-luminosity magnetars (Suzuki & Maeda 2021).

4.4. Host SED modelling

Using the SDSS photometry magnitude (see Table A.1) and after taking into account the contribution of the Milky Way reddening at a redshift of z = 0.065, the absolute magnitude of $M_g = -14.47 \pm 0.24$ mag of the host galaxy of SN 2021lwz points to a very faint dwarf galaxy. We modelled the observed spectral energy distribution (SED) (black data points in Fig. 13) with the software package *Prospector* version 1.3 (Leja et al. 2017)[15]. We assumed a Chabrier IMF (Chabrier 2003) and approximated the star formation history (SFH) by a linearly increasing SFH at early times followed by an exponential decline at late times (functional form $t \times \exp(-t/\tau)$, where t is the age of the SFH episode and τ is the e-folding timescale). The model is attenuated with the Calzetti et al. (2000) model. The priors of the model parameters were set identically to those used by Schulze et al. (2021). Figure 13 shows the observed SED (black data points) and its best fit (grey curve). The SED is adequately described by a galaxy template with a mass of $10^{6.66^{+0.35}_{-0.37}}$ $M_\odot$, and a star-formation rate of $0.04^{+0.03}_{-0.02}$ $M_\odot$ yr^{-1}.

The mass and the star formation rate are comparable to common star-forming galaxies of that stellar mass (grey band in Fig. 14; Elbaz et al. 2007)[16], and they are also similar to those of the host-galaxy populations of SNe from the PTF survey (Schulze et al. 2018) albeit at the very-low-mass end of the observed distribution. The data relative to USSNe are compiled in Table J.1.

As a consistency check, we computed a plot similar to the one shown in Fig. 13, without taking into account the emission lines. We find that the galaxy mass is almost unchanged. On the other hand the SFR departs from a factor of ten from the one discussed in the text and shown in Fig. 14. The new reduced chi-square is also higher. All these points make us confident that, despite the low number of data points, the fit shown in Fig. 13

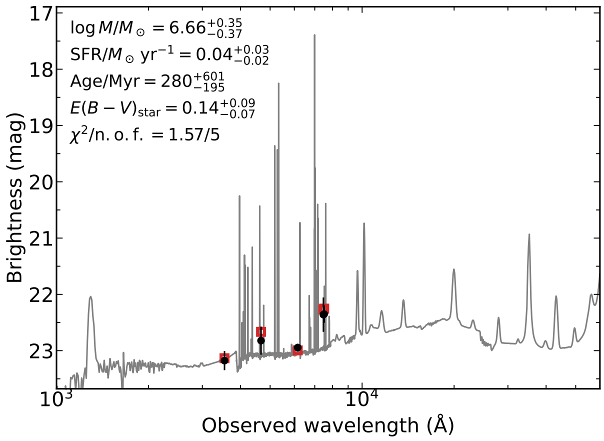

Fig. 13. Spectral energy distribution of the host galaxy from 1000 to 60 000 Å (black dots). The solid line displays the best-fitting model of the SED. The red squares represent the model-predicted magnitudes. The fitting parameters are shown in the upper left corner. The abbreviation n.o.f. stands for the number of filters. The five measurements given in Table A.1 are considered, hence the value of this parameter. Note that the representative wavelengths of the two i-band filters are very similar.

[15] *Prospector* uses the *flexible stellar population synthesis* (*FSPS*) code (Conroy et al. 2009) to generate the underlying physical model and *Python-fsps* (Foreman-Mackey et al. 2014) to interface with *FSPS* in *Python*. The *FSPS* code also accounts for the contribution from the diffuse gas based on the *Cloudy* models from Byler et al. (2017). We use the dynamic nested sampling package *dynasty* (Speagle 2020) to sample the posterior probability.

[16] The relationship between star formation and galaxy mass shown in Fig. 14 is based on results from Brinchmann et al. (2004) and is valid at $z \sim 0$.

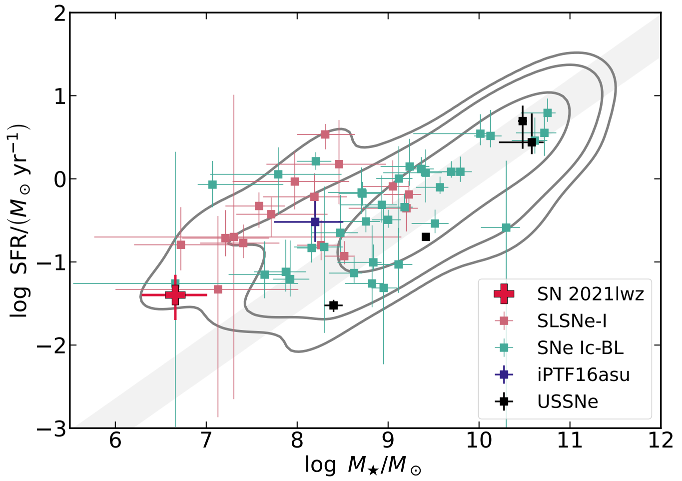

Fig. 14. Star formation rate and stellar mass of SN 2021lwz's host galaxy (dark red) in the context of the CCSN sample from PTF. From the PTF sample, the host properties of iPTF16asu, SNe Ic-BL, and SLSNe-I at $z < 0.2$ are highlighted. SN 2021lwz's host lies in the expected parameter space but at the low-mass end of observed mass distribution. Its specific star formation rate (SFR/mass) is larger than that of the main sequence of star-forming galaxies from SDSS at $z \sim 0$ (grey band; Elbaz et al. 2007 and references therein) by ~1.5 dex, meaning that is a starburst galaxy. The contours indicate the region encircling 68, 90, and 95% of the sample.

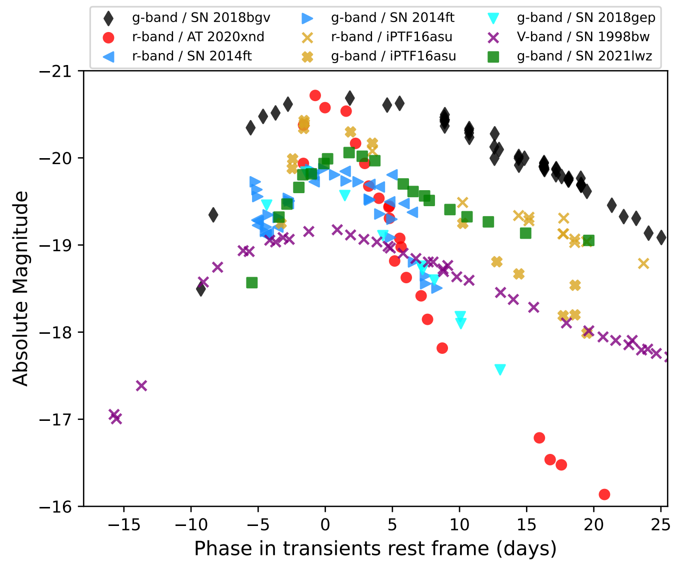

Fig. 15. Rest frame light curves of the fast rising transients ($t_{\rm rise,rf}$ ~< 10 days) and of SN 1998bw ($t_{\rm rise,rf} \sim 20$ days) listed in Table 3. The symbols and colours identify the sources, and the filters used are defined in the legend. The filters were chosen to take into account the redshift of each source for a fairer comparison, except for iPTF 16asu and SN 2014ft, for which g-band and r-band data are shown to demonstrate the rapid increase of these transients. The magnitudes are corrected for the Milky Way extinction, but not for any contribution from the hosts.

including the emission lines is better suited than one not including them would be.

5. Discussion

Based on our previous modelling and analysis, the nature of SN 2021lwz is not clear. This very fast evolving explosion ($t_{\rm rise} \sim 7$ days, rest frame), with a low ejecta mass ($M_{\rm ej} \sim 0.2\,M_\odot$), was drawn from a very-low-brightness ($M_g = -14.47 \pm 0.24$ mag), low-mass ($10^{6.66^{+0.35}_{-0.37}}\,M_\odot$) dwarf galaxy with an SFR ($0.04^{+0.03}_{-0.02}\,M_\odot$ yr^{-1}) about ten times larger than that typical of star-forming galaxies.

To discuss SN 2021lwz in a broader context, in Fig. 15 we show the rest frame light curves of the different types of transients listed in Table 3; namely SN 2018bgv (SLSN-I), SN 1998bw (peculiar Ic-BL), AT 2020xnd (LFBOT), SN 2014ft (USSN), iPTF16asu (SL Ic-BL), and SN 2018gep (SL Ic-BL). As was done for SN 2021lwz, if the photometry was not already corrected for the extinction contribution from our Galaxy, it was done using Schlafly & Finkbeiner (2011). Insofar as possible, the filters were chosen by taking into account of the redshift of each source so that the rest frame wavelength ranges covered strongly overlap.

From the comparison of their rising time parameters given in Table 3, all these transients, except SN 1998bw, reach their maximum light in about ten days or less. SN 2018bgv appears slightly more energetic than SN 2021lwz. On the other side of the absolute magnitude range, SN 1998bw is the less energetic transient. SN 2018bgv and SN 1998bw, whose rest frame rising times are about twice (or more) that of SN 2021lwz, both have smooth light curves, which decrease slightly faster than that of SN 2021lwz. The light curves of iPTF 16asu, SN 2014ft, AT 2020xnd SN 2028gep, SN 2014ft, and SN 2021lwz all strongly overlap with each other before and up to a few days after maximum light. A few days after peak, however, the light curves of AT 2020xnd, SN 2014ft, and SN 2018gep decrease faster than the light curves of SN 2021lwz. All in all, the light curve of iPTF 16asu is the one that looks more similar to the one of SN 2021lwz.

5.1. H-poor SLSNe

SN 2018bgv is the fastest evolving (~10 days rest frame) Type-W SLSN-I reported in the literature. It peaks close to ~−20.7 mag. It is therefore very interesting for comparisons with SN 2021lwz. While we did not model it with our magnetar model, the light curve and a spectral sequence were studied in detail by Lunnan et al. (2020). From blackbody fit analyses of the light curve, the authors reported a photosphere temperature close to 11 000 K and a blackbody radius close to 2×10^{15} cm a few days after the peak, i.e. a photopshere with a radius about two times larger than and a temperature similar to those of the SN 2021lwz photosphere at similar phases. Close to the peak the velocity of the photosphere of SN 2018bgv appears to be about 1.5 times the velocity estimated for SN 2021lwz. A fit of the light curve with the magnetar spin-down model using MOSFIT infers an ejecta mass of $M_{\rm ej} \sim 1.3\,M_\odot$, i.e. about five times higher than the one of SN 2021lwz from our modelling estimate, which suggests the conditions behind the explosions of SN 2018bgv and SN 2021lwz are different.

As discussed in Sect. 3.1 SN 2018bgv provides a relatively good match with SN 2021lwz close to maximum light, but this is obtained at a lower redshift ($z \sim 0.055$) than the redshift of SN 2021lwz. This is mainly because SNID tries to adjust the archetypal W-shape feature attributed to O II, before and close to maximum light, observed in many Type I SLSNe. Indeed, and as discussed in Sect. 4.1, for H-poor SLSNe the typical absorption spectral features expected to be observed before maximum light, between 4000 and 5000 Å (see Könyves-Tóth & Seli 2023,

Table 3. Data on additional sources used for comparison with SN 2021lwz.

Object Name	RA	Dec	Type	z	$t_{rise,rf}$ $^{(a)}$ [days]	band	$m^{(b)}$ [mag]	M $^{(c)}$ [mag]	References
SN 2018bgv	11:02:30.29	+55:35:55.79	SLSN-I	0.08	∼10	g	17.06	−20.71	1
AT 2020xnd	22:20:02.03	−02:50:25.27	LFBOT	0.2442	<5.6	r	19.56	−20.72	2
SN 2014ft	23:33:27.95	+33:38:46.14	USSN	0.1868	$\sim5.9^{(d)}$	r	19.62	−20.06	3
iPTF 16asu	12:59:09.28	+13:48:09.19	SL Ic-BL	0.187	∼4	g	19.14	−20.53	4, 5
SN 2018gep	16:43:48.22	+41:02:43.37	SL Ic-BL	0.031875	5.4 ± 0.5	g	15.93	−19.84	6
SN 1998bw	19:35:03.310	−52:50:44.81	Ic-BL	0.008499	∼17	V	13.60	−19.33	7, 8
SN 2021lwz	09:44:47.40	+34:42:44.25	?	0.065	∼7	g	17.25	−20.08	This work

Notes. $^{(a)}$ $t_{rise,rf}$ is the estimated rising time from explosion in the rest frame; $^{(b)}$ difference magnitude; $^{(c)}$ absolute magnitude; $^{(d)}$ here, we refer to the second and largest peaks as discussed in De et al. (2018). (1) Lunnan et al. (2020); (2) Perley et al. (2021a); (3) De et al. (2018); (4) Whitesides et al. (2017); (5) Wang & Gan (2022); (6) Pritchard et al. (2021); (7) Galama et al. (1998); (8) Patat et al. (2001).

Fig. 1) in Type 15bn (e.g. Fe III) and in Type W (e.g. O II), are not detected in the pre-maximum spectra of SN 2021lwz. Instead, C II, O I, Na I, Mg II, Si II, Ca II, Ti II, and Fe II are included to reproduce the shape of these spectra, and this is despite the fact that from the estimates of the photosphere temperature ($T_{phot} \approx$ 20 000 K) and the photosphere velocities (10 000 $< v_{phot} <$ 15 000 km/s before maximum light), one would expect features from a W-Type SLSN-I (see Könyves-Tóth 2022, Fig. 7). We point out, however, that the conditions for these lines to appear are likely limited to a more stringent temperature range of $T_{phot} \sim$ 14 000–16 000 K once spectral modelling effects, which are not included in the SYN++ modelling, are taken into account (see Saito et al. 2024). However, the study provided by Aamer et al. (2025), obtained on a sample larger than the one used by Könyves-Tóth & Seli (2023) suggests a continuum of spectral properties; hence, the differences of spectral profiles in Type I SLSNe may not correspond to physically different types of events. In this larger sample Fe II lines appear to be an important spectral marker formed near the photosphere, which is also found for SN 2021lw.

5.2. LFBOTs

The LFBOT AT 2020xnd and SN 2021lwz are peaking at about similar absolute magnitudes (see Fig. 15), but AT 2020xnd is a faster evolving event than SN 2021lwz, mainly because it has a higher initial pulsar luminosity, assuming a magnetar model. Two spectra of AT 2020xnd at phases close to +5 days and +7 days after maximum light are publicly available in the WISeREP repository[17]. From the point of view of the photosphere evolution, the two very smooth spectra, which are continuum blue flux dominated, do not show any strong absorption features, unlike those seen in the spectra of SN 2021lwz after maximum light (see Fig. 3). This observational fact, combined with the analysis of their light curves using the magnetar model (for AT 2020xnd, see Table 2 in Omand & Sarin 2024), suggests that AT 2020xnd and SN 2021lwz differ in nature and do not pertain to the same class of transients. This conclusion is sustained by a visual comparison among some spectra of SN 2021lwz and some of SN 2020xnd and SN 2018cow, as shown in Fig. 16. The spectral evolution of SN 2021lwz shows absorption features stronger than those observed in the spectra of AT 2020xnd and AT 2018cow, which, in comparison, look almost featureless.

[17] URL to AT 2020xnd public spectra in WISeREP, https://www.wiserep.org/object/18199

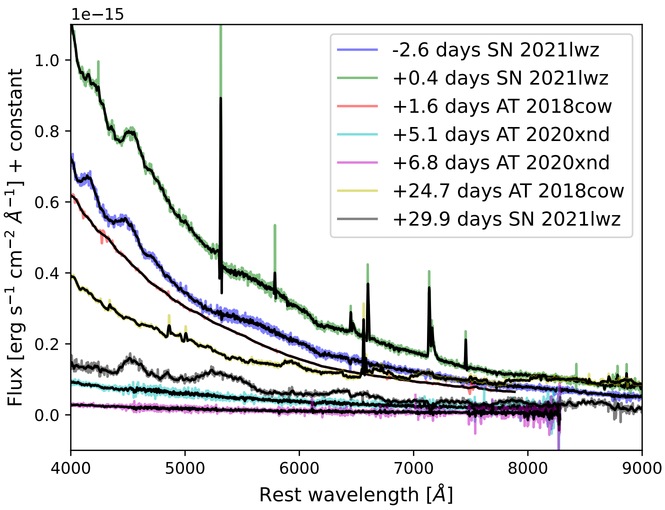

Fig. 16. Some spectra of FBOTs AT 2020xnd and AT 2018cow are shown for comparison with some of the spectra obtained on SN 2021lwz (see Fig. 3). All the spectra were smoothed using a Savitzky–Golay low pass filter.

5.3. USSN

SN 2014ft has been observed, studied, and classified by De et al. (2018) as a USSN that likely formed a compact neutron star binary. It is recognised as the first ever detection of a USSN (Hijikawa et al. 2019), while previous studies of fast evolving Type Ic-BL SNe such as SN 2005ek (Drout et al. 2013) and SN 2010X (Kasliwal et al. 2010) pointed out the existence of this class of objects. Posterior to these works, SN 2019dge (or ZTF18abfcmjw) was added to this class of transients, as discussed by Yao et al. (2020). More recently, SN 2023zaw has been shown to be a fast evolving USSN of very low ejecta mass ($M_{ej} \sim 0.07\,M_\odot$; Das et al. 2024; Moore et al. 2025).

SN 2014ft was modelled using the REDBACK (Sarin et al. 2024) magnetar-driven SN model in Omand & Sarin (2024). SN 2021lwz and SN 2014ft have very similar light curves, both peaking at absolute magnitudes close to −20.1 mag (Fig. 15), and similar fast rising times of the order of six to seven days (see Table 3). Assuming the magnetar-driven SN model is appropriate to describe both explosions, the posterior parameters from the light curve modelling both infer very low ejecta of the same order (∼0.15−0.25 $M_\odot$) and SN explosion energies of the same order (∼2−6 × 10^{49} erg). The main difference is that SN 2021lwz has an initial spin-down luminosity about 100 times higher than the one of SN 2014ft, and a spin-down timescale that is about ten times faster. The braking index of both explosions being of the same order (~4.5), this results in SN 2021lwz having a total rotational energy an order of magnitude higher than SN 2014ft.

During the first 30 hours after explosion, SN 2014ft showed He II λ4686 Å lines in three spectra (see Fig. 3A in De et al. 2018). Such early spectra are not available for SN 2021lwz; therefore, we do not know if a similar feature was present very early in its photosphere. A similar feature is not detected in the earliest spectra available on SN 2021lwz obtained about five to seven days after the explosion (see Fig. 3). Hints of He I, but not of He II, are only suggested by the modelling analysis in the post-peak spectra of SN 2021lwz. At maximum light, the spectra of SN 2021lwz and SN 2014ft show common ionisation atomic lines from Ca II, Mg II, Fe II, Ti II, Si II, C II, and O I (see our SYN++ analysis and Fig. 5B in De et al. 2018), but absorption lines of P III (while not unambiguous) and Na I observed in the spectrum of SN 2021lwz were not detected in the spectrum of SN 2014ft. The distinct temperatures of the photosphere estimated for each SN close to maximum light, with $T_{phot} \approx$ 20 000 K for SN 2021lwz (this work) and $T_{phot} \approx$ 11 000 K for SN 2014ft (Fig. 4B in De et al. 2018), may explain this difference. Before and near maximum light, SN 2021lwz has a steeper continuum than SN 2014ft, showing that it is hotter and likely comes from a more energetic event; this inference is consistent with the one provided by the modelling of the light curves. In the near-maximum spectra, around 5000 Å, SN 2014ft shows a 'basin-shaped' feature similarly to SN 2015bn, while this is missing from the spectra of SN 2021lwz, again most probably because of the difference in the temperatures. The post-maximum spectral lines are somewhat more similar, but SN 2014ft is still cooler than SN 2021lwz.

Finally, we point out that, contrary to the high specific SFR of the host of SN 2021lwz, the specific SFR of USSNe shown in Fig. 14 is generally lower than, or about equal to, the average expected value for typical star-forming galaxies (grey band). The stellar masses of the USSNe galaxies are also two to four orders of magnitudes higher than the mass of SN 2021lwz's host. The statistics are low, however, with only four hosts of USSNe. With all the arguments put together, it is not clear if SN 2021lwz has been ultra-stripped or not, the main argument in favour of an ultra-stripped process being that it has a low ejecta mass, which is indeed the case for SN 2014ft.

5.4. Typical H-poor stripped envelope SNe

Hydrogen-poor, core-collapse SESNe, of Types Ib, Ic, and Ic-BL, are well studied in the optical (e.g. Drout et al. 2011; Taddia et al. 2019), the NIR (e.g. Shahbandeh et al. 2022), and at radio wavelengths (Srinivasaragavan et al. 2024). As discussed previously, our post-peak optical spectral modelling hints at a marginal detection of He I and the possible 1.0830 μm line. Possible connections and a continuity between typical Type Ib and Ic has been discussed, with no clear results about residual detections of He I in optical spectra (e.g. Hachinger et al. 2012; Piro & Morozova 2014; Prentice et al. 2018; Dessart et al. 2020; Williamson et al. 2021). More recently, Shahbandeh et al. (2022) presented the analysis of 75 NIR spectra of 34 SESNe with the aim of discussing NIR strong He I lines: λ1.0830 μm and λ2.0581 μm. In all spectra, except a few outliers, most of the absorption-line features observed close to 1 μm can be explained by a combination of strong lines (C I λ1.0693 μm, He I λ1.0830 μm, and Mg II λ1.0927 μm), and the authors concluded that there is no distinct difference between He-poor and He-rich groups in this wavelength range. On the other hand, by analysing the 2 μm features the authors showed one can clearly distinguish He-rich (optical IIb/Ib) from He-poor (optical Ic/Ic-BL) SESNe and computed SESNe templates using a principal component analysis. The +13 day templates of such He-rich and He-poor SNe are shown in Fig. 4 for illustration. A comparison with the +12.6 day NIR spectrum of SN 2021lwz, which optical spectral modelling points out to be Type Ic-like, disfavours the presence of residual He I. Actually, in the vicinity of the He I 2 μm feature, the spectrum of SN 2021lwz looks flatter than the He-poor template, as does the spectrum of the peculiar Type Ic-BL, SN 1998bw.

Additional arguments making SN 2021lwz peculiar with respect to SESNe are the following. It is more luminous at the peak than the majority of these objects (see e.g. our plot in Fig. 1 for a direct comparison with Type Ic and Ic-BL absolute magnitudes). It has a low-mass ejecta (as inferred from our multi-band modelling), $M_{ej} \sim 0.24^{+0.04}_{-0.04}\,M_{\odot}$, which is in contradiction with typical ^{56}Ni ejecta masses of $M_{Ni} \approx 0.2$ and $0.5\,M_{\odot}$ for SNe Ib/c and SN Ic-BL, respectively (Drout et al. 2011), as well as with the ejecta masses expected for these two Types of SNe, of order $M_{ej} \approx 2$ and $5\,M_{\odot}$, respectively (Drout et al. 2011; Taddia et al. 2019). More recently Rodríguez et al. (2023) studied 191 stripped-envelope SNe, including 50 Ib SNe and 96 Ic SNe, of which 26 are Ic-BL SNe. Compared to that SN Ib/Ic/Ic-BL sample, SN 2021lwz is at least ten times more luminous at the peak than average (2.7 and 4.5×10^{42} erg s^{-1} for Ib and Ic/Ic-BL, respectively). Its ejecta mass is about ten times lower than the average (2.6 $M_{\odot}$), and it is also lower than the minimum ejecta mass (0.5 $M_{\odot}$), making it a low-occurrence event in the bottom tail of the distribution.

5.5. Comparisons with peculiar Type Ic-BL SN 1998bw

Before and close to maximum light, the photosphere of SN 2021lwz looks more similar to a normal Type Ic SN than to any other type, with C II, O I, Na I, Mg II, Si II, Ca II, Ti II, and Fe II lines identified in its earliest spectrum (see Sect. 4.1); the velocity of the spectral features and of the photosphere are close to those of a Type Ic SN. Slightly broader optical spectral features observed after peak suggest that SN 2021lwz could have evolved closer to a Type Ic-BL. Before maximum light, the SYN++ modelling actually shows that the photosphere velocity of SN 2021lwz is not extraordinarily high (~15 000 km/s), and the broadness parameter *aux* (see values displayed in Table F.1) point to a normal Type Ic. After maximum light, the input *aux* parameter value had to be higher to adjust the formation of several broader spectral features, meaning that SN 2021lwz may be closer to the limit of a Ic-BL. Still, after the peak the best match is obtained with LSQ12dlf, which is an SLSN-I showing velocity lines below the 30 000 km/s seen in classic Ic-BL SNe. The match with the +14 day and +16 day spectra of SN 1998bw are not too bad above $\lambda \sim 5300$ Å, but they are relatively poor at lower wavelengths. Some attempts to fit the −3.4 day Keck spectrum of SN 2021lwz with early spectra of SN 1998bw proved unsuccessful. Some differences between the NIR spectra of both transients can also be seen in Fig. 4. All in all, SN 2021lwz seems to be an SLSN of Ic-SL type after the peak.

5.6. Comparisons with fast-evolving, luminous Type Ic-BL iPTF16asu

iPTF 16asu, whose origin is not yet well understood, was first discussed by Whitesides et al. (2017). It is a luminous, rapidly evolving, stripped-envelope SN peaking at $M_g \sim -20.5$ mag. With a rest frame rise time estimated to be of ∼4 days, it appears to be a faster evolving event than SN 2021lwz. Contrary to SN 2021lwz, which looks like a Type Ic SN before peak, iPTF 16asu shows a relatively featureless blue continuum; however, contrary to SN 2021lwz, iPTF 16asu shows Ic-BL features after the peak (see some spectra shown in Fig. 17 for comparison).

In Appendix I we present the fit of the multi-band light curve of iPTF 16asu using the same software, model, and priors as for SN 2021lwz (see Sect. 4.3 for details). The light curve fit is shown in Fig. I.1, and the posterior is shown in Fig. I.2. From our modelling, the estimated SN explosion energy of iPTF 16asu is about 30 times stronger than the one of SN 2021lwz, which could explain the optical spectral differences before the peak.

More in-depth light curve modelling of iPTF 16asu was discussed by Wang et al. (2019). In Sect. 4.2 we discuss the difficulty of modelling the light curve of SN 2021lwz using the Arnett model; similarly, the analysis proposed by these authors underlined the difficulty of modelling the light curve of iPTF 16asu with radioactive heating (^{56}Ni-only), as well as the magnetar ^{56}Ni models. Our modelling of iPTF 16asu and SN 2021lwz includes a fraction of nickel in the ejecta mass (see Eq. (9) in Omand & Sarin 2024), which, given the total ejecta mass estimate $M_{\rm ej} \approx 0.17\,M_\odot$ and $M_{\rm ej} \approx 0.24\,M_\odot$, of each object, respectively, means the nickel mass would be excessively low. Energetically speaking, we find that these low ejecta masses are both associated with rotational energies of the same order ($E_{\rm rot} = \frac{n-1}{2} L_0 t_{\rm SD}$). The light curves of both events are very similar and peak at absolute magnitudes close to ∼−20.3 mag. They also have fast rising times sharing a common parameter space ($t_{\rm rise} \lesssim 7$ days; see Table 3 and Fig. 1). The g-band data plotted in Fig. 15 show the steep increase of iPTF 16asu, while the r-band data show a decreasing light curve very similar to the one of SN 2021lwz.

The interpretation of the results obtained by Wang et al. (2019) and an additional modelling of the light curves were proposed by Wang & Gan (2022). The construction of the theoretical bolometric light curve was revised, and the authors find that the magnetar plus ^{56}Ni model can now account for the photometry of iPTF 16asu, with a peak luminosity inferred from the theoretical light curve of $\sim 1.06 \times 10^{44}$ erg. The best-fit value for the ejecta mass is $M_{\rm ej} = 0.19\,M_\odot$, and the best-fit parameter of the nickel mass is $M_{\rm Ni} = 0.029\,M_\odot$. Some results very close to the best-fit parameters were obtained with our modelling of the multi-light curve of SN 2021lwz. All these results possibly make SN 2021lwz part of a class of rare, rapidly evolving ($t_{\rm rise,restframe}$ <∼ 1 week), luminous Type Ic-BL SNe ($M_g \sim -20$ mag or slightly higher), similar to iPTF 16asu (see Wang & Gan 2022); however, SN 2021lwz is an intermediate-velocity ($v_{\rm phot} \sim 15\,000$ km s^{-1}) Type Ic/Ic-BL object, while iPTF 16asu is a high-velocity Type Ic-BL SN after the peak.

5.7. Comparisons with fast-evolving luminous Type Ic-BL SN 2018gep

SN 2018gep (see Ho et al. 2019; Leung et al. 2021; Pritchard et al. 2021) is another rapidly rising (1.4 ± 0.1 mag h^{-1} during the first hours just after explosion), stripped envelope SN, spectroscopically classified as a Ic-BL SN (see Ho et al. 2019). As a Ic-BL SN, its light curve shows similarities with that of iPTF 16asu (see Pritchard et al. 2021 and our Fig. 15). With a total fast rise time of $t_{\rm rise,V} = 5.6 \pm 0.5$ days after explosion and a peak absolute magnitude of $M_V = -19.53 \pm 0.23$ mag, it shares a common locus with iPTF 16asu and SN 2021lwz

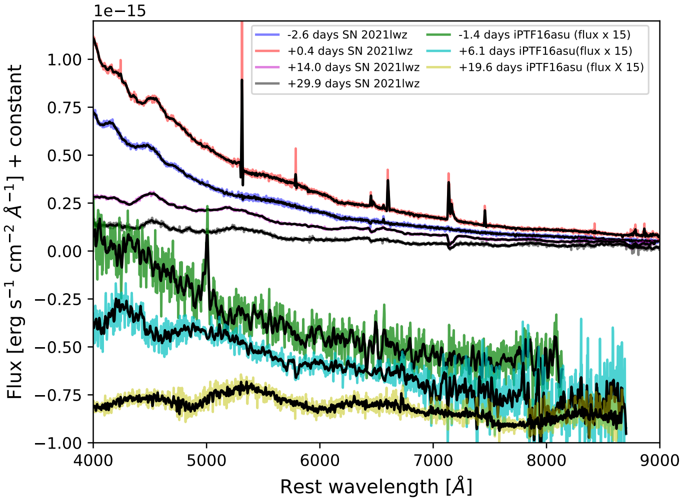

Fig. 17. Some spectra of iPTF 16asu and SN 2021lwz are shown for comparison with some of the spectra obtained on SN 2021lwz (see Fig. 3). All the spectra were smoothed using a Savitzky–Golay low pass filter.

on the extreme side of the distribution of a Ic-BL SN in this parameter space (see Pritchard et al. 2021 and our Fig. 1). The spectra obtained during the first three days after explosion are blue-dominated spectra showing smooth absorption features of highly ionised elements (CIV, O III, CIII) and a very hot photosphere decreasing from ∼40 000 K to ∼20 000 K. Then, the W-Type signature attributed to O II and C II absorption lines observed in many Type I SLSNe before and around the peak is visible in the spectra of SN 2018gep obtained during the fourth day after explosion (see Fig. 11 in Ho et al. 2019). This marks the main difference with SN 2021lwz spectra, whereby this signature is interpreted differently given the assumed redshift of SN 2021lwz (see Sect. 4.1). Globally, all these comparisons suggest that SN 2021lwz has characteristics of, and is probably closely related to, many of these classes, and it is therefore most likely some kind of transitional event.

5.8. Prospects and final remarks

An interesting test of the magnetar scenario for luminous, fast-evolving objects is non-thermal emission. These objects could emit luminous X-ray (Kotera et al. 2013; Metzger et al. 2014; Murase et al. 2015) and radio emission (Murase et al. 2015; Omand et al. 2018; Eftekhari et al. 2021; Murase et al. 2021; Omand et al. 2025a), similarly to PTF 10hgi (Eftekhari et al. 2019; Law et al. 2019; Mondal et al. 2020) or SN 2012au (Stroh et al. 2021) after a few years, but on timescales of a few weeks to a year. There could also be bright infrared emission on short timescales due to dust heated by the PWN (Omand et al. 2019), although this emission would likely fade quickly as the dust cools. The dominant non-thermal component can be predicted, in principle, from the nebular spectrum of the SN, since line emission is sensitive to the underlying PWN spectrum (Omand & Jerkstrand 2023); however, these models are not currently capable of reproducing nebular spectra on timescales of less than a year.

The multi-dimensional structure of these magnetar-driven SNe could show strong clumping due to Rayleigh–Taylor instabilities between the nebula and ejecta (Blondin & Chevalier 2017; Suzuki & Maeda 2017). When $E_{\rm rot} > E_{\rm exp}$, such as in SN 2021lwz, the shock can break through the ejecta

(Blondin & Chevalier 2017), leading to a decrease in the ejecta acceleration efficiency. This process, known as blowout, has been inferred to happen in the Crab Nebula (Omand et al. 2025b). Clumpy ejecta can cause polarisation if the clump size is large enough (Tanaka et al. 2017), but we do not currently know how to determine the clump size distribution from the inferred engine properties of the SN.

It has been proposed by Zou & Cheng (2018) that Type I SLSNe and Type Ic-BL could be produced by jets. If so, they would both show strong polarisation from early times. We point out that for SN 2021lwz our non-detections contribute to ruling out this scenario. Additionally, if the energy was injected into the ejecta early, most of it would accelerate the ejecta instead of contributing to the luminosity (Suzuki & Maeda 2021).

6. Conclusions

SN 2021lwz is a peculiar luminous SN at a redshift of $z = 0.065$ with an absolute magnitude of $M_g \approx -20.1$ (AB system). It was discovered in a very-low-brightness ($M_g = -14.47 \pm 0.24$ mag), low-mass ($10^{6.66^{+0.35}_{-0.37}}\,M_\odot$) dwarf galaxy with an SFR ($0.04^{+0.03}_{-0.02}\,M_\odot\,\mathrm{yr}^{-1}$) about ten times larger than that typical of star-forming galaxies. An extensive analysis and modelling of the photometry, spectroscopy, and polarimetry data of the SN, followed by comparisons with SNe of well-known types and with rarer transients, consistently leads to the following results:

- SN 2021lwz shows a rapidly evolving and luminous optical light curve. The bolometric light curve rises over about seven days to a peak luminosity of about 5×10^{43} erg/s at a rate of 0.2 mag day^{-1} close to the peak. From the intrinsic bolometric luminosity, we derive $T_{\mathrm{rise},10\%} = 6.1 \pm 0.3$ days and $T_{\mathrm{rise,exp}} = 4.9 \pm 0.3$ days (rest frame).
- SN 2021lwz has a low-mass ejecta of $M_{\mathrm{ej}} \sim 0.24\,M_\odot$ (as from the magnetar model) with estimated velocities of $\sim$15 000 km s^{-1} at -3.4 days and of $\sim$7500 km s^{-1} after the peak at +13..2 and +29.1 days, respectively. Near the peak the photosphere has a temperature of $\sim$18 000 K, a radius of $\sim 10^{15}$ cm, and a velocity of $\sim$10 000 km s^{-1}, which is consistent with the ejecta velocity.
- If SN 2021lwz is a magnetar-driven SN, it is expected to have an initial luminosity of $L_0 \approx 3 \times 10^{45}$ erg s^{-1}; a spin-down timescale of $t_{\mathrm{SD}} \approx 1$ day; and an ejecta mass, a final ejecta scale velocity, and a photospheric temperature at the peak similar to the ones reported above.
- The magnetar-driven model leads to a very short diffusion time of $t_{\mathrm{diff}} \sim 5$ days due to the low ejecta mass, a bolometric peak timescale of $\sim$7 days, and a g-band peak timescale of $\sim$10 days; the discrepancy between these values (Fig. 12) is consistent with the high photospheric temperature and rapid cooling around the peak (Fig. 7). The SN is expected to have entered the nebular phase on a timescale of $t_{\mathrm{neb}} \approx 27$ days ± 2 but the spectroscopy shows the nebular phase should have started after +30 days. The gamma-ray leakage timescale, t_{leak}, is very long.
- The shape of the photosphere of SN 2021lwz looks close to perfectly spherical and does not show any loss of symmetry between the two phases close to (≈+1.0 days) and after maximum light (≈+19. days). The observed symmetry of the system rules out a jet activity being at the origin of SN 2021lwz.
- Spectroscopically, SN 2021lwz looks like a Type Ic-like SN before maximum light. After maximum light some velocity lines may be a bit larger, but the post-peak spectrum looks most like an SLSN, and the continuum slope (see Fig. 3) is much more like an SLSN that a Ic-BL, which is usually much redder from line blanketing.
- Given its spectroscopic properties and the low ejecta mass needed to model its light curve, SN 2021lwz does not match with many core-collapse H-poor SNe types.
- Using the magnetar model, the low ejecta mass of SN 2021lwz and its light curve shape possibly make it a USSN, but this is not possible to demonstrate with the data at hand.
- SN 2021lwz shows similarities with the peculiar Type Ic-BL SN 1998bw, but some differences in their rise time and absolute magnitudes at their peak and in their NIR spectra suggest they are two different types of objects.
- The light curve and multi-band light curve modelling of SN 2021lwz suggest it shares similarities with iPTF 16asu, and with SN 2018gep. The three sources show continuum blue-dominated spectra before maximum light, even though SN 2021lwz shows spectral features pointing to a Type Ic-like SNe, while iPTF 16asu and SN 2018gep do not. A possible explanation is that iPTF 16asu and SN 2018gep are more energetic explosions quickly rising to higher photosphere temperatures than SN 2021lwz.

In conclusion, SN 2021lwz is an uncommon transient showing many similarities with several classes of transients and with rare transients. It may be an interesting example showing how differences in ejecta mass and engine parameters could produce a wide range of engine-driven SESNe.

With the advent of new high-cadence large-scale deeper surveys such as the Vera C. Rubin observatory Large Synoptic Survey Telescope (LSST; Ivezić et al. 2019), very early detections of bright, low-redshift events similar to SN 2021lwz may help us to better understand such phenomena. Similarly, data obtained with the *Euclid* satellite (Euclid Collaboration: Mellier et al. 2025) should be helpful for tackling such problems. The observing strategy is not optimised for transient science, but the Quick Data Release 1 has proven to be useful for early- and late-type detections of some SNe (see Duffy et al. 2026).

Data availability

For science reproducibility purposes, the photometry and the spectra presented in this work are available via WISEReP[18] (Yaron & Gal-Yam 2012). Table C.1 is available at the CDS via `https://cdsarc.cds.unistra.fr/viz-bin/cat/J/A+A/710/A367`

Acknowledgements. The authors would like to thank the anonymous referee for her/his insightfull and constructive comments, Sheng Yang, Anna Ho and Ósmar Rodríguez for helpful discussions and inputs. We thank Rosa Clavero and David Morate for their kind support on the NOT. We thank George Khorenzhev (Space Research Institute, Russian Academy of Sciences) for contributing to some observations. F.P. and C.G.C. acknowledge support from the Spanish Ministerio de Ciencia, Innovación y Universidades (MICINN) under grant numbers PID2022-141915NB-C21. R.K.T. has been supported by the NKFIH/OTKA FK-134432 grant of the National Research, Development and Innovation Office of Hungary (NKFIH). C. M. B. O. acknowledges support from the Royal Society (grant Nos. DHF-R1-221175 and DHF-ERE-221005). N. Sarin acknowledges support from the Kavli foundation. T.-W.C. acknowledges the Yushan Fellow Program by the Ministry of Education, Taiwan for the financial support (MOE-111-YSFMS-0008-001-P1). T.K. acknowledges support from the Research Council of Finland project 360274. Based on observations obtained with the Samuel Oschin Telescope 48-inch and the 60-inch Telescope at the Palomar Observatory as part of the *Zwicky* Transient Facility project. ZTF is supported by the National Science Foundation under Grant No. AST-2034437

[18] `https://www.wiserep.org/object/18321`

and a collaboration including Caltech, IPAC, the Weizmann Institute of Science, the Oskar Klein Center at Stockholm University, the University of Maryland, Deutsches Elektronen-Synchrotron and Humboldt University, the TANGO Consortium of Taiwan, the University of Wisconsin at Milwaukee, Trinity College Dublin, Lawrence Livermore National Laboratories, IN2P3, University of Warwick, Ruhr University Bochum, Cornell University, and Northwestern University. Operations are conducted by COO, IPAC, and UW. *Zwicky* Transient Facility access was supported by Northwestern University and the Center for Interdisciplinary Exploration and Research in Astrophysics (CIERA). The ZTF forced-photometry service was funded under the Heising-Simons Foundation grant No. 12540303 (PI: Graham). SED Machine is based upon work supported by the National Science Foundation under Grant No. 1106171. The Gordon and Betty Moore Foundation, through both the Data-Driven Investigator Program and a dedicated grant, provided critical funding for SkyPortal. Based on observations made with the Nordic Optical Telescope (NOT), owned in collaboration by the University of Turku and Aarhus University, and operated jointly by Aarhus University, the University of Turku and the University of Oslo, representing Denmark, Finland and Norway, the University of Iceland and Stockholm University at the Observatorio del Roque de los Muchachos, La Palma, Spain, of the Instituto de Astrofísica de Canarias. The data presented here were obtained in part with ALFOSC, which is provided by the Instituto de Astrofísica de Andalucia (IAA) under a joint agreement with the University of Copenhagen and NOT. Some of the data were obtained during CAT service observation Spanish time. ALFOSC polarimetry imaging data of SN2020ank and alibration data were retrieved from the NOT public archive. The Liverpool Telescope is operated on the island of La Palma by Liverpool John Moores University in the Spanish Observatorio del Roque de los Muchachos of the Instituto de Astrofísica de Canarias with financial support from the UK Science and Technology Facilities Council. This work has made use of data from the Asteroid Terrestrial- impact Last Alert System (ATLAS) project. The Asteroid Terrestrial-impact Last Alert System (ATLAS) project is primarily funded to search for near earth asteroids through NASA grants NN12AR55G, 80NSSC18K0284, and 80NSSC18K1575; by-products of the NEO search include images and catalogues from the survey area. This work was partially funded by Kepler/K2 grant J1944/80NSSC19K0112 and HST GO-15889, and STFC grants ST/T000198/1 and ST/S006109/1. The ATLAS science products have been made possible through the contributions of the University of Hawaii Institute for Astronomy, the Queen s University Belfast, the Space Telescope Science Institute, the South African Astronomical Observatory, and The Millennium Institute of Astrophysics (MAS), Chile. Lasair is supported by the UKRI Science and Technology Facilities Council and is a collaboration between the University of Edinburgh (grant ST/N002512/1) and Queen's University Belfast (grant ST/N002520/1) within the LSST:UK Science Consortium. SNID is Copyright (C) 1999-2007 Stéphane Blondin and John L. Tonry, and is available under the GNU General Public License. This research made use of the Transient Name Server (TNS) which is the official IAU mechanism for reporting new astronomical transients such as supernova candidates, As of January 1, 2016. This research made use of Legacy Survey Data Release 10 data. The Legacy Surveys consist of three individual and complementary projects: the Dark Energy Camera Legacy Survey (DECaLS; Proposal ID #2014B-0404; PIs: David Schlegel and Arjun Dey), the Beijing-Arizona Sky Survey (BASS; NOAO Prop. ID #2015A-0801; PIs: Zhou Xu and Xiaohui Fan), and the Mayall z-band Legacy Survey (MzLS; Prop. ID #2016A-0453; PI: Arjun Dey). DECaLS, BASS and MzLS together include data obtained, respectively, at the Blanco telescope, Cerro Tololo Inter-American Observatory, NSF's NOIRLab; the Bok telescope, Steward Observatory, University of Arizona; and the Mayall telescope, Kitt Peak National Observatory, NOIRLab. The Legacy Surveys project is honored to be permitted to conduct astronomical research on Iolkam Du'ag (Kitt Peak), a mountain with particular significance to the Tohono O'odham Nation. NOIRLab is operated by the Association of Universities for Research in Astronomy (AURA) under a cooperative agreement with the National Science Foundation. This project used data obtained with the Dark Energy Camera (DECam), which was constructed by the Dark Energy Survey (DES) collaboration. Funding for the DES Projects has been provided by the U.S. Department of Energy, the U.S. National Science Foundation, the Ministry of Science and Education of Spain, the Science and Technology Facilities Council of the United Kingdom, the Higher Education Funding Council for England, the National Center for Supercomputing Applications at the University of Illinois at Urbana-Champaign, the Kavli Institute of Cosmological Physics at the University of Chicago, Center for Cosmology and Astro-Particle Physics at the Ohio State University, the Mitchell Institute for Fundamental Physics and Astronomy at Texas A&M University, Financiadora de Estudos e Projetos, Fundacao Carlos Chagas Filho de Amparo, Financiadora de Estudos e Projetos, Fundacao Carlos Chagas Filho de Amparo a Pesquisa do Estado do Rio de Janeiro, Conselho Nacional de Desenvolvimento Cientifico e Tecnologico and the Ministerio da Ciencia, Tecnologia e Inovacao, the Deutsche Forschungsgemeinschaft and the Collaborating Institutions in the Dark Energy Survey. The Collaborating Institutions are Argonne National Laboratory, the University of California at Santa Cruz, the University of Cambridge, Centro de Investigaciones Energeticas, Medioambientales y Tecnologicas-Madrid, the University of Chicago, University College London, the DES-Brazil Consortium, the University of Edinburgh, the Eidgenossische Technische Hochschule (ETH) Zurich, Fermi National Accelerator Laboratory, the University of Illinois at Urbana-Champaign, the Institut de Ciencies de l'Espai (IEEC/CSIC), the Institut de Fisica d'Altes Energies, Lawrence Berkeley National Laboratory, the Ludwig Maximilians Universitat Munchen and the associated Excellence Cluster Universe, the University of Michigan, NSF's NOIRLab, the University of Nottingham, the Ohio State University, the University of Pennsylvania, the University of Portsmouth, SLAC National Accelerator Laboratory, Stanford University, the University of Sussex, and Texas A&M University. The Legacy Surveys imaging of the DESI footprint is supported by the Director, Office of Science, Office of High Energy Physics of the U.S. Department of Energy under Contract No. DE-AC02-05CH1123, by the National Energy Research Scientific Computing Center, a DOE Office of Science User Facility under the same contract; and by the U.S. National Science Foundation, Division of Astronomical Sciences under Contract No. AST-0950945 to NOAO.

References

Aamer, A., Nicholl, M., Gomez, S., et al. 2025, MNRAS, 541, 2674
Agudo, I., Amati, L., An, T., et al. 2023, A&A, 675, A201
Ahn, C. P., Alexandroff, R., Allende Prieto, C., et al. 2012, ApJS, 203, 21
Ambikasaran, S., Foreman-Mackey, D., Greengard, L., Hogg, D. W., & O'Neil, M. 2015, IEEE Trans. Pattern Anal. Mach. Intell., 38, 252
Arcavi, I., Wolf, W. M., Howell, D. A., et al. 2016, ApJ, 819, 35
Arnett, W. D. 1982, ApJ, 253, 785
Ashton, G., Hübner, M., Lasky, P. D., et al. 2019, ApJS, 241, 27
Barbarino, C., Sollerman, J., Taddia, F., et al. 2021, A&A, 651, A81
Bellm, E. C., Kulkarni, S. R., Barlow, T., et al. 2019a, PASP, 131, 068003
Bellm, E. C., Kulkarni, S. R., Graham, M. J., et al. 2019b, PASP, 131, 018002
Bertin, E. 2010, Astrophysics Source Code Library [record ascl:1010.068]
Bertin, E., & Arnouts, S. 2010, Astrophysics Source Code Library [record ascl:1010.064]
Bertin, E., Mellier, Y., Radovich, M., et al. 2002, ASP Conf. Ser., 281, 228
Blagorodnova, N., Neill, J. D., Walters, R., et al. 2018, PASP, 130, 035003
Blondin, J. M., & Chevalier, R. A. 2017, ApJ, 845, 139
Blondin, S., & Tonry, J. L. 2007, ApJ, 666, 1024
Breeveld, A. A., Landsman, W., Holland, S. T., et al. 2011, AIP Conf. Ser., 1358, 373
Brinchmann, J., Charlot, S., White, S. D. M., et al. 2004, MNRAS, 351, 1151
Buchner, J., Georgakakis, A., Nandra, K., et al. 2014, A&A, 564, A125
Byler, N., Dalcanton, J. J., Conroy, C., & Johnson, B. D. 2017, ApJ, 840, 44
Calzetti, D., Armus, L., Bohlin, R. C., et al. 2000, ApJ, 533, 682
Chabrier, G. 2003, PASP, 115, 763
Chambers, K. C., Magnier, E. A., Metcalfe, N., et al. 2016, ArXiv e-prints [arXiv:1612.05560]
Chen, Z. H., Yan, L., Kangas, T., et al. 2023a, ApJ, 943, 41
Chen, Z. H., Yan, L., Kangas, T., et al. 2023b, ApJ, 943, 42
Conroy, C., Gunn, J. E., & White, M. 2009, ApJ, 699, 486
Coughlin, M. W., Bloom, J. S., Nir, G., et al. 2023, ApJS, 267, 31
Cushing, M. C., Vacca, W. D., & Rayner, J. T. 2004, PASP, 116, 362
Das, K. K., Fremling, C., Kasliwal, M. M., et al. 2024, ApJ, 969, L11
De, K., Kasliwal, M. M., Ofek, E. O., et al. 2018, Science, 362, 201
Dekany, R., Smith, R. M., Riddle, R., et al. 2020, PASP, 132, 038001
Dessart, L., Yoon, S.-C., Aguilera-Dena, D. R., & Langer, N. 2020, A&A, 642, A106
Drake, A. J., Djorgovski, S. G., Mahabal, A., et al. 2009, ApJ, 696, 870
Drout, M. R., Soderberg, A. M., Gal-Yam, A., et al. 2011, ApJ, 741, 97
Drout, M. R., Soderberg, A. M., Mazzali, P. A., et al. 2013, ApJ, 774, 58
Drout, M. R., Chornock, R., Soderberg, A. M., et al. 2014, ApJ, 794, 23
Duffy, C., Cappellaro, E., Botticella, M. T., et al. 2026, A&A, 711, A38
Eftekhari, T., Berger, E., Margalit, B., et al. 2019, ApJ, 876, L10
Eftekhari, T., Margalit, B., Omand, C. M. B., et al. 2021, ApJ, 912, 21
Elbaz, D., Daddi, E., Le Borgne, D., et al. 2007, A&A, 468, 33
Euclid Collaboration (Mellier, Y., et al.) 2025, A&A, 697, A1
Fitzpatrick, E. L. 1999, PASP, 111, 63
Foreman-Mackey, D., Sick, J., & Johnson, B. 2014, https://doi.org/10.5281/zenodo.12157
Fremling, C. 2021, TNSTR, 2021–1564, 1
Fremling, C., Sollerman, J., Taddia, F., et al. 2016, A&A, 593, A68
Galama, T. J., Vreeswijk, P. M., van Paradijs, J., et al. 1998, Nature, 395, 670
Gehrels, N., Chincarini, G., Giommi, P., et al. 2004, ApJ, 611, 1005
Gomez, S., Berger, E., Nicholl, M., Blanchard, P. K., & Hosseinzadeh, G. 2022, ApJ, 941, 107
Gomez, S., Nicholl, M., Berger, E., et al. 2024, MNRAS, 535, 471

Graham, M. J., Kulkarni, S. R., Bellm, E. C., et al. 2019, PASP, 131, 078001
Guillochon, J., Nicholl, M., Villar, V. A., et al. 2018, ApJS, 236, 6
Hachinger, S., Mazzali, P. A., Taubenberger, S., et al. 2012, MNRAS, 422, 70
Heiles, C. 2000, AJ, 119, 923
Hijikawa, K., Kinugawa, T., Yoshida, T., & Umeda, H. 2019, ApJ, 882, 93
Ho, A. Y. Q., Goldstein, D. A., Schulze, S., et al. 2019, ApJ, 887, 169
Ho, A. Y. Q., Perley, D. A., Gal-Yam, A., et al. 2023, ApJ, 949, 120
Hogg, D. W., Baldry, I. K., Blanton, M. R., & Eisenstein, D. J. 2002, ArXiv e-prints [arXiv:astro-ph/0210394]
Hosseinzadeh, G., Berger, E., Metzger, B. D., et al. 2022, ApJ, 933, 14
Inserra, C., Smartt, S. J., Jerkstrand, A., et al. 2013, ApJ, 770, 128
Inserra, C., Bulla, M., Sim, S. A., & Smartt, S. J. 2016, ApJ, 831, 79
Ivezić, Ž., Kahn, S. M., Tyson, J. A., et al. 2019, ApJ, 873, 111
Kaiser, N., Burgett, W., Chambers, K., et al. 2010, SPIE Conf. Ser., 7733, 77330E
Kasen, D., & Bildsten, L. 2010, ApJ, 717, 245
Kasliwal, M. M., Kulkarni, S. R., Gal-Yam, A., et al. 2010, ApJ, 723, L98
Kerzendorf, W. E., & Sim, S. A. 2014, MNRAS, 440, 387
Khatami, D. K., & Kasen, D. N. 2024, ApJ, 972, 140
Kim, Y. L., Rigault, M., Neill, J. D., et al. 2022, PASP, 134, 024505
Könyves-Tóth, R. 2022, ApJ, 940, 69
Könyves-Tóth, R., & Seli, B. 2023, ApJ, 954, 44
Kornilov, M. V., Semenikhin, T. A., & Pruzhinskaya, M. V. 2023, MNRAS, 526, 1822
Kotera, K., Phinney, E. S., & Olinto, A. V. 2013, MNRAS, 432, 3228
Law, C. J., Omand, C. M. B., Kashiyama, K., et al. 2019, ApJ, 886, 24
Lawrence, A., Warren, S. J., Almaini, O., et al. 2007, MNRAS, 379, 1599
Leja, J., Johnson, B. D., Conroy, C., van Dokkum, P. G., & Byler, N. 2017, ApJ, 837, 170
Leloudas, G., Maund, J. R., Gal-Yam, A., et al. 2017, ApJ, 837, L14
Leung, S.-C., Fuller, J., & Nomoto, K. 2021, ApJ, 915, 80
Lunnan, R., Yan, L., Perley, D. A., et al. 2020, ApJ, 901, 61
Masci, F. J., Laher, R. R., Rusholme, B., et al. 2023, ArXiv e-prints [arXiv:2305.16279]
Metzger, B. D., Vurm, I., Hascoët, R., et al. 2014, MNRAS, 437, 703
Mondal, S., Bera, A., Chandra, P., et al. 2020, MNRAS, 498, 3863
Moore, T., Gillanders, J. H., Nicholl, M., et al. 2025, ApJ, 980, L44
Murase, K., Kashiyama, K., Kiuchi, K., et al. 2015, ApJ, 805, 82
Murase, K., Omand, C. M. B., Coppejans, D. L., et al. 2021, MNRAS, 508, 44
Nagao, T., Maeda, K., Mattila, S., et al. 2024, A&A, 687, L17
Nakaoka, T., Maeda, K., Yamanaka, M., et al. 2021, ApJ, 912, 30
Nakar, E., & Piro, A. L. 2014, ApJ, 788, 193
Nakar, E., & Sari, R. 2010, ApJ, 725, 904
Nicholl, M. 2018, Res. Notes Am. Astron. Soc., 2, 230
Nicholl, M., Berger, E., Margutti, R., et al. 2016a, ApJ, 828, L18
Nicholl, M., Berger, E., Smartt, S. J., et al. 2016b, ApJ, 826, 39
Nicholl, M., Guillochon, J., & Berger, E. 2017, ApJ, 850, 55
Oke, J. B., Cohen, J. G., Carr, M., et al. 1995, PASP, 107, 375
Omand, C. M. B., & Jerkstrand, A. 2023, A&A, 673, A107
Omand, C. M. B., & Sarin, N. 2024, MNRAS, 527, 6455
Omand, C. M. B., Kashiyama, K., & Murase, K. 2018, MNRAS, 474, 573
Omand, C. M. B., Kashiyama, K., & Murase, K. 2019, MNRAS, 484, 5468
Omand, C. M. B., Sarin, N., & Lamb, G. P. 2025a, MNRAS, 539, 1908
Omand, C. M. B., Sarin, N., & Temim, T. 2025b, MNRAS, 536, 408
Ostriker, J. P., & Gunn, J. E. 1971, ApJ, 164, L95
Patat, F., Cappellaro, E., Danziger, J., et al. 2001, ApJ, 555, 900
Patterson, M. T., Bellm, E. C., Rusholme, B., et al. 2019, PASP, 131, 018001
Perley, D. A. 2019, PASP, 131, 084503
Perley, D. A., Ho, A. Y. Q., Yao, Y., et al. 2021a, MNRAS, 508, 5138
Perley, D. A., Yao, Y., Chen, T., et al. 2021b, TNS Classif. Rep., 2021–1649, 1
Piro, A. L. 2015, ApJ, 808, L51
Piro, A. L., & Morozova, V. S. 2014, ApJ, 792, L11
Planck Collaboration I. 2020, A&A, 641, A1
Prentice, S. J., Mazzali, P. A., Pian, E., et al. 2016, MNRAS, 458, 2973
Prentice, S. J., Ashall, C., Mazzali, P. A., et al. 2018, MNRAS, 478, 4162
Pritchard, T. A., Bensch, K., Modjaz, M., et al. 2021, ApJ, 915, 121
Pursiainen, M., Childress, M., Smith, M., et al. 2018, MNRAS, 481, 894
Quimby, R. M., Kulkarni, S. R., Kasliwal, M. M., et al. 2011, Nature, 474, 487
Rau, A., Kulkarni, S. R., Law, N. M., et al. 2009, PASP, 121, 1334
Rigault, M., Neill, J. D., Blagorodnova, N., et al. 2019, A&A, 627, A115
Rodríguez, Ó., Maoz, D., & Nakar, E. 2023, ApJ, 955, 71
Romero-Shaw, I. M., Talbot, C., Biscoveanu, S., et al. 2020, MNRAS, 499, 3295
Roming, P. W. A., Kennedy, T. E., Mason, K. O., et al. 2005, Space Sci. Rev., 120, 95
Saito, S., Tanaka, M., Mazzali, P. A., et al. 2024, ApJ, 967, 13
Sarin, N., Hübner, M., Omand, C. M. B., Setzer, C. N., et al. 2024, MNRAS, 531, 1203
Schlafly, E. F., & Finkbeiner, D. P. 2011, ApJ, 737, 103
Schulze, S., Krühler, T., Leloudas, G., et al. 2018, MNRAS, 473, 1258
Schulze, S., Yaron, O., Sollerman, J., et al. 2021, ApJS, 255, 29
Shahbandeh, M., Hsiao, E. Y., Ashall, C., et al. 2022, ApJ, 925, 175
Shingles, L., Smith, K. W., Young, D. R., et al. 2021, TNSAN, 7, 1
Smith, K. W., Smartt, S. J., Young, D. R., et al. 2020, PASP, 132, 085002
Soker, N. 2024, Open J. Astrophys., 7, 31
Speagle, J. S. 2020, MNRAS, 493, 3132
Srinivasaragavan, G. P., Yang, S., Anand, S., et al. 2024, ApJ, 976, 71
Steele, I. A., Smith, R. J., Rees, P. C., et al. 2004, SPIE Conf. Ser., 5489, 679
Stroh, M. C., Terreran, G., Coppejans, D. L., et al. 2021, ApJ, 923, L24
Suzuki, A., & Maeda, K. 2017, MNRAS, 466, 2633
Suzuki, A., & Maeda, K. 2021, ApJ, 908, 217
Taddia, F., Sollerman, J., Fremling, C., et al. 2019, A&A, 621, A71
Tanaka, M., Tominaga, N., Morokuma, T., et al. 2016, ApJ, 819, 5
Tanaka, M., Maeda, K., Mazzali, P. A., et al. 2017, ApJ, 837, 105
Thomas, R. C., Nugent, P. E., & Meza, J. C. 2011, PASP, 123, 237
Tonry, J. L., Denneau, L., Flewelling, H., et al. 2018a, ApJ, 867, 105
Tonry, J. L., Denneau, L., Heinze, A. N., et al. 2018b, PASP, 130, 064505
Vacca, W. D., Cushing, M. C., & Rayner, J. T. 2003, PASP, 115, 389
van der Walt, S., Crellin-Quick, A., & Bloom, J. 2019, J. Open Source Softw., 4, 1247
Vurm, I., & Metzger, B. D. 2021, ApJ, 917, 77
Wang, S.-Q., & Gan, W.-P. 2022, ApJ, 928, 114
Wang, L., Wheeler, J. C., & Höflich, P. 1997, ApJ, 476, L27
Wang, S. Q., Wang, L. J., Dai, Z. G., et al. 2015, ApJ, 799, 107
Wang, L. J., Wang, X. F., Cano, Z., et al. 2019, MNRAS, 489, 1110
West, S. L., Lunnan, R., Omand, C. M. B., et al. 2023, A&A, 670, A7
Whitesides, L., Lunnan, R., Kasliwal, M. M., et al. 2017, ApJ, 851, 107
Williamson, M., Kerzendorf, W., & Modjaz, M. 2021, ApJ, 908, 150
Wilson, J. C., Henderson, C. P., Herter, T. L., et al. 2004, SPIE Conf. Ser., 5492, 1295
Woosley, S. E. 2010, ApJ, 719, L204
Yan, L., Quimby, R., Gal-Yam, A., et al. 2017, ApJ, 840, 57
Yan, L., Perley, D. A., Schulze, S., et al. 2020, ApJ, 902, L8
Yan, S., Wang, X., Gao, X., et al. 2023, ApJ, 959, L32
Yao, Y., De, K., Kasliwal, M. M., et al. 2020, ApJ, 900, 46
Yaron, O., & Gal-Yam, A. 2012, PASP, 124, 668
Zou, Y.-C., & Cheng, K. S. 2018, PASA, 35, e032

Table A.1. Photometry of SN 2021lwz's host galaxy.

Survey Telescope/Instrument	Band	Brightness (mag)
CFHT/MegaPrime	*u*	23.23 ± 0.16
SDSS	*g*	22.86 ± 0.24
CFHT/MegaPrime	*r*	22.97 ± 0.05
Pan-STARRRS	*i*	22.37 ± 0.15
SDSS	*i*	22.38 ± 0.30

Table B.1. Spectra obtained on SN 2021lwz.

Instrument	Observation Date [UT]	rest frame phase (relative to g-band)
P60/SEDM	2021-05-11T04:07:47	-5.4
Keck/LRIS[(*)]	2021-05-13T05:40:20	-3.4
P60/SEDM	2021-05-15T04:07:59	-1.6
NOT/ALFOSC	2021-05-15T22:02:58	-0.9
Keck/LRIS	2021-05-16T09:40:23	-0.5
NOT/ALFOSC	2021-05-18T21:57:56	1.9
P60/SEDM	2021-05-24T04:00:59	6.8
P60/SEDM	2021-05-28T04:04:46	10.6
P60/SEDM	2021-05-30T05:48:20	12.5
Keck/NIRES	2021-05-30T07:15:08	12.6
NOT/ALFOSC	2021-05-30T21:58:39	13.2
P60/SEDM	2021-06-13T04:15:04	25.6
NOT/ALFOSC	2021-06-16T21:20:28	29.1

Notes. [(*)] spectrum publicly available on TNS.

Appendix A: Host photometry table

The measurements in the different bands of the host galaxy of SN 2021lwz discussed in Sect. 2.1, are given in Table A.1. The magnitudes are not corrected for extinction.

Appendix B: Spectroscopy table

The log of the spectroscopy obtained on SN 2021lwz discussed in Sect. 2.2 is given in Table,B.1. The rest frame phase relative to the g-band filter is given using MJD_{max} = 59350 days.

Appendix C: Photometry table

All the photometry obtained on SN 2021lwz is given in Table C.1.

Table C.1. Photometric data of SN 2021lwz.

MJD	Phase[a] (days)	Filter	Magnitude (mag)	Telescope
59344.2	-6.7	g	18.76 ± 0.03	ZTF
59344.2	-6.7	r	19.21 ± 0.04	ZTF
59345.3	-5.6	o	18.69 ± 0.05	ATLAS
59346.2	-4.7	r	18.35 ± 0.02	ZTF
59346.3	-4.6	g	18.01 ± 0.04	ZTF
59347.0	-3.9	sdssg	17.86 ± 0.03	LT
59347.0	-3.9	sdssr	18.22 ± 0.04	LT
59347.0	-3.9	sdssi	18.39 ± 0.08	LT
59347.0	-3.9	sdssu	17.85 ± 0.16	LT
59347.0	-3.9	sdssz	18.73 ± 0.28	LT
59347.4	-3.5	UVW1	17.41 ± 0.04	Swift
59347.4	-3.5	U	17.31 ± 0.05	Swift
59347.4	-3.5	B	17.54 ± 0.09	Swift
59347.4	-3.5	UVW2	17.89 ± 0.04	Swift

Table C.1. continued.

MJD	Phase[a] (days)	Filter	Magnitude (mag)	Telescope
59347.4	-3.5	V	17.97 ± 0.18	Swift
59347.4	-3.5	UVM2	17.55 ± 0.03	Swift
59347.9	-3.0	sdssg	17.67 ± 0.03	LT
59347.9	-3.0	sdssr	18.01 ± 0.03	LT
59347.9	-3.0	sdssi	18.44 ± 0.03	LT
59347.9	-3.0	sdssu	17.37 ± 0.04	LT
59347.9	-3.0	sdssz	18.64 ± 0.07	LT
59348.2	-2.7	r	17.96 ± 0.02	ZTF
59348.2	-2.7	g	17.53 ± 0.01	ZTF
59348.3	-2.6	c	17.77 ± 0.02	ATLAS
59348.3	-2.6	UVW1	17.34 ± 0.04	Swift
59348.3	-2.6	U	17.09 ± 0.06	Swift
59348.3	-2.6	B	17.38 ± 0.09	Swift
59348.3	-2.6	UVW2	17.84 ± 0.04	Swift
59348.3	-2.6	V	17.91 ± 0.23	Swift
59348.3	-2.6	UVM2	17.45 ± 0.04	Swift
59348.9	-2.0	sdssg	17.52 ± 0.03	LT
59348.9	-2.0	sdssr	17.86 ± 0.03	LT
59348.9	-2.0	sdssi	18.23 ± 0.03	LT
59348.9	-2.0	sdssu	17.16 ± 0.01	LT
59348.9	-2.0	sdssz	18.48 ± 0.05	LT
59349.3	-1.6	UVW1	17.32 ± 0.04	Swift
59349.3	-1.6	U	17.15 ± 0.06	Swift
59349.3	-1.6	B	17.34 ± 0.08	Swift
59349.3	-1.6	UVW2	17.9 ± 0.04	Swift
59349.3	-1.6	V	17.3 ± 0.14	Swift
59349.3	-1.6	UVM2	17.52 ± 0.04	Swift
59349.3	-1.6	o	17.93 ± 0.03	ATLAS
59349.9	-1.0	sdssg	17.4 ± 0.03	LT
59349.9	-1.0	sdssr	17.73 ± 0.04	LT
59349.9	-1.0	sdssi	18.1 ± 0.03	LT
59349.9	-1.0	sdssu	17.1 ± 0.05	LT
59349.9	-1.0	sdssz	18.29 ± 0.05	LT
59350.2	-0.7	g	17.34 ± 0.01	ZTF
59350.2	-0.7	r	17.74 ± 0.02	ZTF
59350.3	-0.6	UVW1	17.21 ± 0.05	Swift
59350.3	-0.6	U	17.01 ± 0.06	Swift
59350.3	-0.6	B	17.29 ± 0.1	Swift
59350.3	-0.6	UVW2	17.86 ± 0.05	Swift
59350.3	-0.6	V	17.31 ± 0.18	Swift
59350.3	-0.6	UVM2	17.55 ± 0.06	Swift
59351.9	1.0	sdssg	17.27 ± 0.03	LT
59351.9	1.0	sdssr	17.56 ± 0.03	LT
59351.9	1.0	sdssi	17.86 ± 0.05	LT
59351.9	1.0	sdssu	16.96 ± 0.03	LT
59351.9	1.0	sdssz	18.12 ± 0.09	LT
59352.3	1.4	o	17.65 ± 0.05	ATLAS
59352.9	2.0	sdssg	17.31 ± 0.07	LT
59352.9	2.0	sdssr	17.61 ± 0.04	LT
59352.9	2.0	sdssi	17.86 ± 0.08	LT
59352.9	2.0	sdssu	17.06 ± 0.05	LT
59352.9	2.0	sdssz	18.2 ± 0.07	LT
59353.9	3.0	sdssg	17.36 ± 0.06	LT
59353.9	3.0	sdssr	17.6 ± 0.04	LT
59353.9	3.0	sdssi	17.86 ± 0.06	LT
59353.9	3.0	sdssu	17.2 ± 0.15	LT
59353.9	3.0	sdssz	18.02 ± 0.12	LT
59354.2	3.3	i	17.95 ± 0.05	ZTF
59354.2	3.3	r	17.69 ± 0.03	ZTF
59354.3	3.4	o	17.72 ± 0.03	ATLAS
59354.4	3.5	UVW1	17.58 ± 0.06	Swift
59354.4	3.5	U	17.21 ± 0.08	Swift
59354.4	3.5	B	17.08 ± 0.1	Swift
59354.4	3.5	UVW2	18.38 ± 0.06	Swift
59354.4	3.5	V	17.28 ± 0.19	Swift

Table C.1. continued.

MJD	Phase[a] (days)	Filter	Magnitude (mag)	Telescope
59354.4	3.5	UVM2	17.94 ± 0.05	Swift
59356.2	5.3	g	17.63 ± 0.03	ZTF
59356.2	5.3	r	17.82 ± 0.04	ZTF
59356.3	5.4	o	17.86 ± 0.04	ATLAS
59356.8	5.9	UVW1	18.11 ± 0.07	Swift
59356.8	5.9	U	17.6 ± 0.09	Swift
59356.8	5.9	B	17.6 ± 0.14	Swift
59356.8	5.9	UVW2	19.08 ± 0.08	Swift
59356.8	5.9	V	17.33 ± 0.2	Swift
59356.8	5.9	UVM2	18.67 ± 0.06	Swift
59357.0	6.1	sdssg	17.72 ± 0.04	LT
59357.0	6.1	sdssr	17.84 ± 0.04	LT
59357.0	6.1	sdssi	18.07 ± 0.04	LT
59357.0	6.1	sdssz	18.13 ± 0.07	LT
59357.9	7.0	sdssg	17.77 ± 0.07	LT
59357.9	7.0	sdssr	17.95 ± 0.03	LT
59357.9	7.0	sdssi	18.1 ± 0.03	LT
59357.9	7.0	sdssu	17.66 ± 0.04	LT
59357.9	7.0	sdssz	18.2 ± 0.05	LT
59358.2	7.3	i	18.08 ± 0.04	ZTF
59358.2	7.3	r	17.93 ± 0.05	ZTF
59358.2	7.3	g	17.82 ± 0.04	ZTF
59359.9	9.0	sdssg	17.92 ± 0.09	LT
59359.9	9.0	sdssr	18.02 ± 0.04	LT
59359.9	9.0	sdssi	18.17 ± 0.03	LT
59359.9	9.0	sdssu	18.27 ± 0.01	LT
59359.9	9.0	sdssz	18.32 ± 0.06	LT
59360.3	9.4	o	18.04 ± 0.06	ATLAS
59361.2	10.3	g	18.01 ± 0.05	ZTF
59362.9	12.0	sdssg	18.07 ± 0.02	LT
59362.9	12.0	sdssr	18.15 ± 0.03	LT
59362.9	12.0	sdssi	18.32 ± 0.03	LT
59362.9	12.0	sdssu	18.38 ± 0.08	LT
59362.9	12.0	sdssz	18.37 ± 0.05	LT
59363.3	12.4	o	18.1 ± 0.04	ATLAS
59364.1	13.2	U	18.7 ± 0.24	Swift
59364.1	13.2	B	17.79 ± 0.21	Swift
59364.1	13.2	UVW2	20.42 ± 0.25	Swift
59364.1	13.2	UVM2	20.2 ± 0.2	Swift
59365.9	15.0	sdssg	18.2 ± 0.03	LT
59365.9	15.0	sdssr	18.26 ± 0.04	LT
59365.9	15.0	sdssi	18.4 ± 0.04	LT
59365.9	15.0	sdssu	18.76 ± 0.09	LT
59365.9	15.0	sdssz	18.46 ± 0.04	LT
59366.9	16.0	UVW1	19.61 ± 0.13	Swift
59366.9	16.0	U	18.72 ± 0.13	Swift
59366.9	16.0	B	18.56 ± 0.2	Swift
59366.9	16.0	UVW2	20.94 ± 0.28	Swift
59367.3	16.4	o	18.06 ± 0.05	ATLAS
59368.5	17.6	UVW1	19.84 ± 0.14	Swift
59368.5	17.6	U	18.72 ± 0.13	Swift
59368.5	17.6	B	18.22 ± 0.15	Swift
59368.5	17.6	UVW2	20.61 ± 0.14	Swift
59368.5	17.6	V	18.21 ± 0.28	Swift
59368.5	17.6	UVM2	20.53 ± 0.12	Swift
59370.9	20.0	UVW1	19.94 ± 0.2	Swift
59370.9	20.0	U	18.73 ± 0.17	Swift
59370.9	20.0	B	18.31 ± 0.21	Swift
59370.9	20.0	UVW2	20.85 ± 0.22	Swift
59370.9	20.0	V	17.79 ± 0.28	Swift
59370.9	20.0	sdssg	18.28 ± 0.03	LT
59370.9	20.0	UVM2	20.5 ± 0.17	Swift
59370.9	20.0	sdssr	18.32 ± 0.03	LT
59370.9	20.0	sdssi	18.45 ± 0.03	LT

Appendix D: Linear polarimetry material

Linear polarimetry of SN 2021lwz obtained with ALFOSC in one of the V-band is shown in Fig. D.1. The log of the polarimetry obtained on SN 2021lwz using ALFOSC on the NOT (see Sect. 2.4) is presented in Table,D.1.

Table C.1. continued.

MJD	Phase[a] (days)	Filter	Magnitude (mag)	Telescope
59370.9	20.0	sdssz	18.5 ± 0.07	LT
59371.3	20.4	o	18.41 ± 0.06	ATLAS
59376.9	26.0	sdssr	18.68 ± 0.04	LT
59376.9	26.0	sdssi	18.71 ± 0.05	LT
59376.9	26.0	sdssz	18.62 ± 0.08	LT
59377.9	27.0	sdssg	18.75 ± 0.04	LT
59377.9	27.0	sdssr	18.74 ± 0.04	LT
59377.9	27.0	sdssi	18.83 ± 0.05	LT
59377.9	27.0	sdssz	18.73 ± 0.07	LT
59381.9	31.0	sdssg	19.05 ± 0.07	LT
59381.9	31.0	sdssr	18.97 ± 0.05	LT
59381.9	31.0	sdssi	19.26 ± 0.12	LT
59381.9	31.0	sdssz	19.04 ± 0.14	LT
59390.2	39.3	r	19.8 ± 0.14	ZTF
59391.2	40.3	r	19.79 ± 0.14	ZTF
59394.2	43.3	r	19.89 ± 0.15	ZTF
59396.2	45.3	r	19.86 ± 0.11	ZTF
59397.2	46.3	r	20.12 ± 0.21	ZTF

Notes. The photometry is reported on the AB system and is not corrected for reddening. The photometry is available on WISEReP (`https://www.wiserep.org/object/18321`) (Yaron & Gal-Yam 2012). Multiple exposures on any given night are averaged to give the values presented here.[(a)] rest frame relative to the g-band maximum (MJD 59350.9).

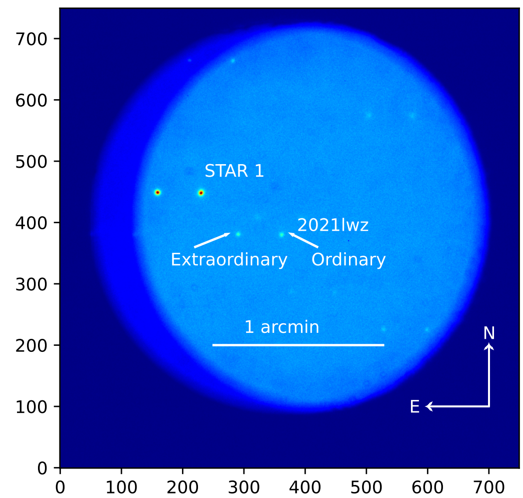

Fig. D.1. Linear polarimetry of SN 2021lwz with ALFOSC in one of the V-band flat-field and bias corrected data frame obtained with the half-wave plate at a position angle of 0.0°. Imaging polarimetry was acquired through half-wave plates positions angles at 0.0°, 22.5°, 45.0° and 67.5°. The calcite plate splits the light from the several objects into Ordinary images and Extraordinary images separated by about 15″ from each other. SN 2021lwz and field star STAR 1, which is used to measure the interstellar polarization component of our Galaxy, are marked in the image.

Appendix E: Fits obtained with SNID

The fits obtained with SNID and discussed in Sect. 3.1 are shown in Fig. E.1

Table D.1. Observations log of the imaging polarimetry observations.

UT Time	Object	Exp. Time [s]	Filter	Seeing [″]
2021-05-17 21:37:36	2021lwz	$1 \times (4 \times 600)$	V	1.9
2021-05-17 22:53:56	HD127769	$2 \times (4 \times 1)$	V	1.5
2021-05-17 22:57:30	GD 319	$2 \times (4 \times 5)$	V	1.3
2021-06-04 21:05:14	2021lwz	$1 \times (4 \times 600)$	V	0.6
2021-06-04 21:26:07	GD 319	$2 \times (4 \times 5)$	V	0.5
2021-06-04 21:30:53	HD127769	$2 \times (4 \times 1)$	V	0.5

Table D.2. Polarimetry results on SN 2021lwz obtained in the V-band Bessel filter.

Date	Source	$\overline{Q}^{(a)}$	$\overline{U}^{(a)}$	$P[\%]^{(a)}$	$P[\%]^{(b)}$	$\theta[^\circ]^{(b)}$	$P[\%]^{(dc}$	$\theta[^\circ]^{(c)}$	$P[\%]^{(d)}$
2021-05-17	BD+52913	0.03	-0.10	0.10±0.09	...	...	...	...	...
–	HD127769	0.45	-1.41	1.48±0.06	1.38±0.11	143.8±2.4	...	...	...
–	STAR 1	-0.06	-0.23	0.23±0.15	0.16±0.18	117.4±32.4	0.16±0.18	26.2±32.4	...
–	2021lwz [(f)]	0.01	0.14	0.15±0.10	0.24±0.14	47.4±15.9	0.24±0.14	136.2±15.9	0.09±0.14
–	...	...	...	...	...	...	...	...	0.0±0.14 [(bc)]
2021-06-04	BD+52913	-0.05	-0.09	0.11±0.15	...	...	...	...	...
–	HD127769	0.52	-2.02	2.09±0.31	2.02±0.34	143.3±4.8	...	...	...
–	STAR 1	-0.33	-0.20	0.39±0.21	0.30±0.26	100.5±24.9	0.30±0.26	9.9±24.9	...
–	2021lwz [(f)]	-0.14	0.20	0.24±0.11	0.30±0.18	53.4±17.2	0.30±0.18	142.8±17.2	0.43±0.18
–	...	...	...	...	...	...	...	...	0.25±0.18[(bc)]

Notes. [(a)] Stokes parameters, $\overline{Q}$ and $\overline{U}$, directly obtained from the ALFOSC data frames Extraordinary and Ordinary images without applying any further corrections. [(ba)] raw data polarization estimates. [(b)] instrumental polarization (IP) corrected. [(c)] instrumental polarization and zero polarization angle (ZPA) corrected. Assuming HD 127769 has a polarization angle of 52.7° in V-band the zero polarization angle, ZPA, estimates are 91.1° and 91.6°, at the first and second epochs, respectively. [(d)] IP and ZPA corrected. [(e)]: IP and ZPA corrected + Milky Way Interstellar polarization corrected with Stokes parameters obtained on star 1[(f)]. [(bc)] bias corrected.

Appendix F: Spectrum modelling with SYN++

The best-fit global parameter values of the SYN++ modelling of SN 2021lwz (see Sect. 4.1)are given in Table,1. The best-fit local SYN++ parameters of the modelled spectra of SN 2021lwz are given in Table F.1.

Appendix G: Bolometric light curve Arnett modelling

In this section we give the details about the bolometric light curve modelling using the Arnett model (see Arnett 1982; Kasen & Bildsten 2010; Woosley 2010; West et al. 2023) which main conclusion (the light curve can't be fit with $M_{ni} \leq M_{ej}$) is given in Sect. 4.2.

Using the `lmfit.minimize` least squares method we retrieve the following parameter values for the radioactive source model: $M_{ej} = 0.3 \pm 0.1$ $M_{\odot}$, $M_{^{56}Ni} = 2.4 \pm 0.3$ $M_{\odot}$, $v_{ej} = 1 \times 10^4$ km s^{-1} (see Sect. 3.6), $E_k \approx 0.2 \times 10^{51}$ erg, $t_{leak} = 22 \pm 3$ days and the diffusion timescale was ≈ 9 days. The resulting best fit model is shown in red in Fig. G.1. Since the total ejecta mass includes the mass of ^{56}Ni these parameter results must be considered to be unphysical.

By re-parameterising the ^{56}Ni mass as a fraction of the ejecta mass we then force the fit to be physical. However, as shown by the dashed red line in Fig. G.1, the fit converges poorly.

We also fit the bolometric light curve with the magnetar model. Parameter values are found to be $M_{ej} = 0.3 \pm 0.07$ $M_{\odot}$, $B_{14} = 1.8 \pm 0.6 \times 10^{14}$ Gauss, $P_{ms} = 5.8 \pm 0.7$, $v_{ej} = 1 \times 10^4$ km s^{-1} (see Sect. 3.6), $t_{leak} = 16 \pm 3$ days, the diffusion timescale ≈ 9 days, and the spindown timescale ≈ 51 days. The resulting best fit parameter model is plotted in blue together with the bolometric light curve in green in Fig. G.1.

Appendix H: Magnetar-driven model of SN 2021lwz

We fit the multi-band light curve of SN 2021lwz shown in Fig. 11 using the software, model, and priors discussed in Sect. 4.3. The posterior is shown in Fig. I.2.

Appendix I: Magnetar-driven model of iPTF16asu

We fit the multi-band light curve of iPTF16asu using the same software, model, and priors as for SN 2021lwz (see Sect. 4.3 for details). The light curve fit is shown in Fig. I.1 and posterior is shown in Fig. I.2.

Appendix J: USSN table

The list of USSNe objects displayed in Sect. 4.4 and their associated properties are given in Table J.1.

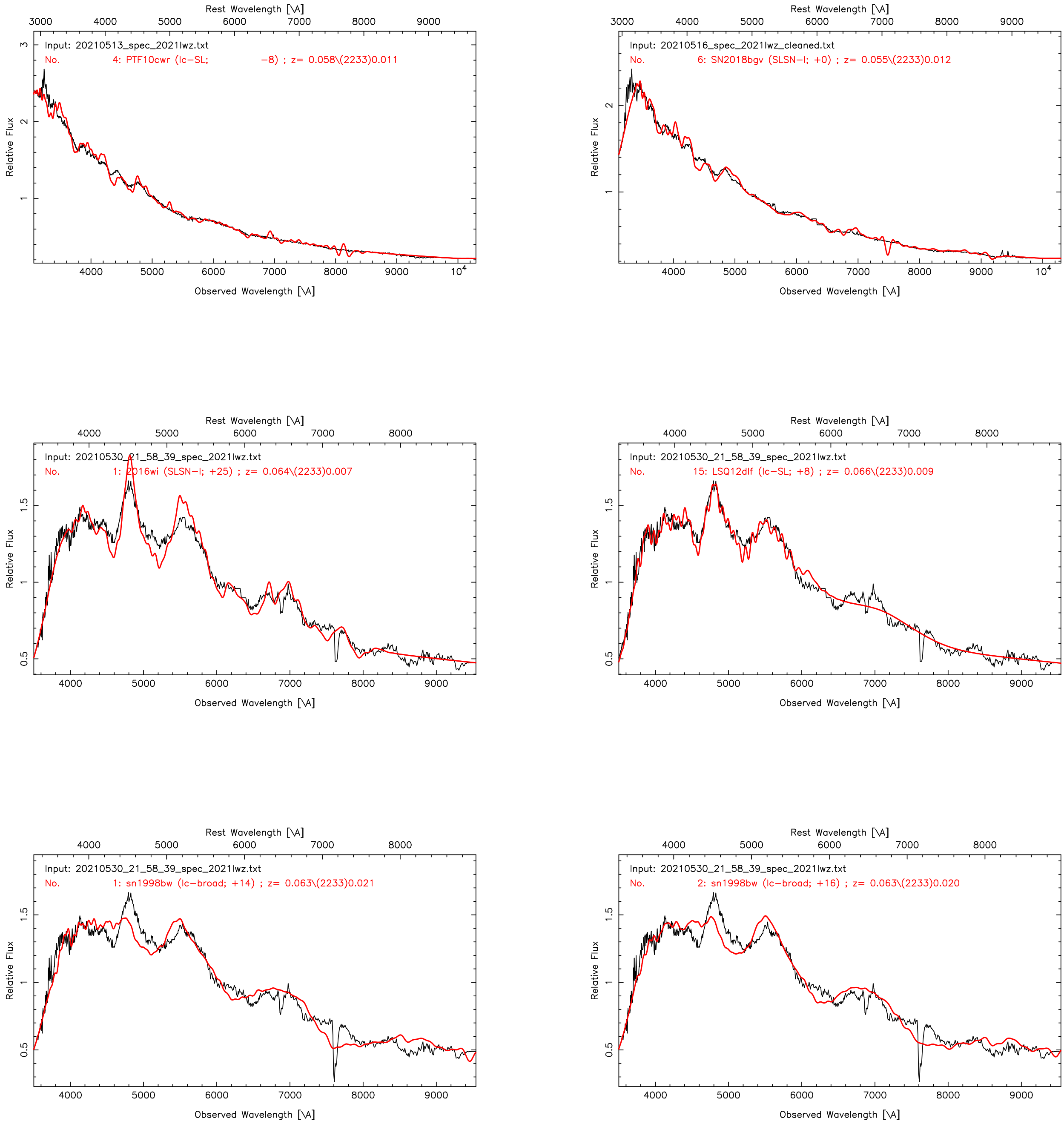

Fig. E.1. Fits of some of the SN 2021lwz spectra using SNID. Top-left: -3.4 days Keck spectrum fit with Type Ic-SL PTF10cwr. Top-right: -0.5 days Keck spectrum fit with fast-rising SLSN-I SN 2018bgv. Middle: example of a post-peak good fit obtained on the ALFOSC +13.2 days spectrum of SN 2021lwz with Type H-poor SLSN SN 2016wi (left), and with Ic-SL SN LSQ12dlf. Bottom: fits obtained on the ALFOSC +13.2 days spectrum using SN 1998bw templates for comparisons.

Table F.1. Best-fit local SYN++ parameters of the modelled spectra of SN 2021lwz.

Ions	He I	C II	O I	Na I	Mg II	Si II	Ca II	Ti II	Fe II
-3.4 days phase									
$\log\tau$		-1.0	-1.0	0.9	-0.5	-0.4	-0.3	-1.6	-0.5
v_{min}		15.0	15.0	15.0	15.0	15.0	15.0	15.0	15.0
v_{max}		50.0	50.0	50.0	50.0	50.0	50.0	50.0	50.0
aux		1.0	1.0	1.0	1.0	1.0	1.0	1.0	1.0
T_{exc}		20.0	20.0	5.0	20.0	20.0	20.0	7.0	12.0
+13.2 days and +29.1 days phase									
$\log\tau$	-0.3	-0.8	-0.3		0.3	0.0	0.0		0.1
v_{min}	7.5	7.5	7.5		7.5	7.5	7.5		7.5
v_{max}	50.0	50.0	50.0		50.0	50.0	50.0		50.0
aux	10.0	5.0	3.0		1.0	2.0	5.0		3.0
T_{exc}	8.0	20.0	8.0		8.0	20.0	15.0		8.0

Notes. The values of v_{min} and v_{max} are given in 1000 km s^{-1}, while T_{exc} is in given in 1000 K.

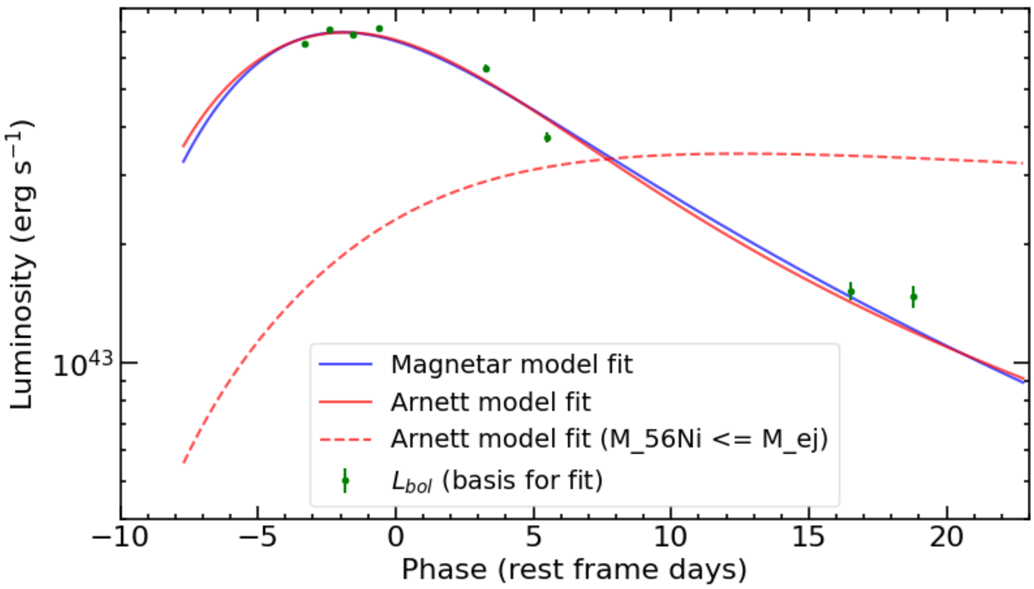

Fig. G.1. SN 2021lwz bolometric light curve in green with its best fit Magnetar (in blue) and Arnett radioactive (in red) source models. If the ^{56}Ni mass is forced to be less than or equal to the ejecta mass then the red dashed line is the best fit one can obtain.

Table J.1. Compilation of the USSNe data.

OBJECT	$MASS_{MED}$	$MASS_{SUP}$	$MASS_{INF}$	SFR_{MED}	SFR_{SUP}	SFR_{INF}	REF.	TYPE
SN2021agco	9.41	9.42	9.41	-0.70	-0.68	-0.72	1	USSN
SN2019dge	8.4	8.5	8.30	-1.52	-1.46	-1.60	2	USSN
SN2019wxt	10.58	10.71	10.22	0.44	0.79	0.30	3	USSN
SN2014ft	10.48	10.53	10.43	0.69	0.88	0.36	4	USSN

Notes. These data are used for discussion in Sect. 4.4. The masses and SFRs are in log units. **References.** (1) Yan et al. (2023); (2) Yao et al. (2020); (3) Agudo et al. (2023); (4) De et al. (2018).

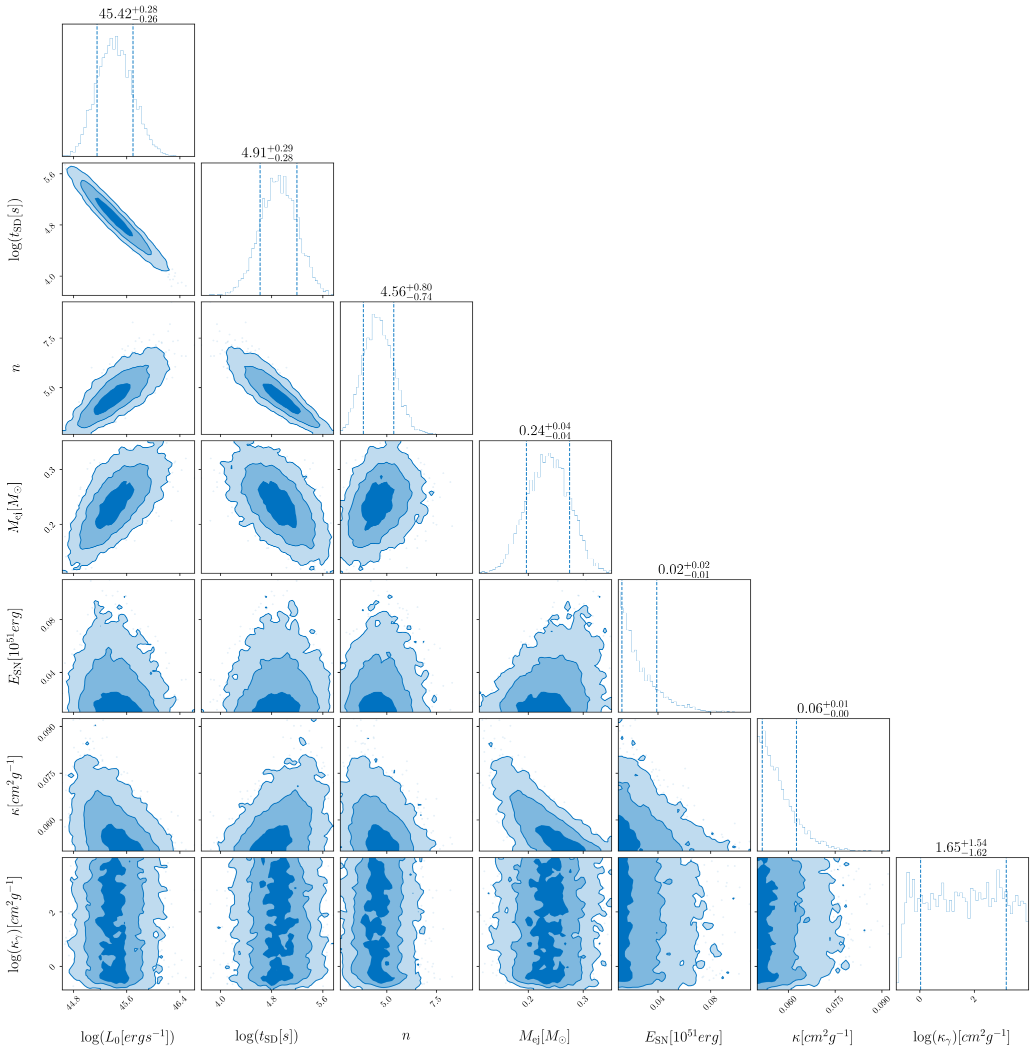

Fig. H.1. Posterior distribution of key physical parameters inferred by the light curve fit shown in Fig. 11. Median values and 1σ uncertainties are given above each parameter.

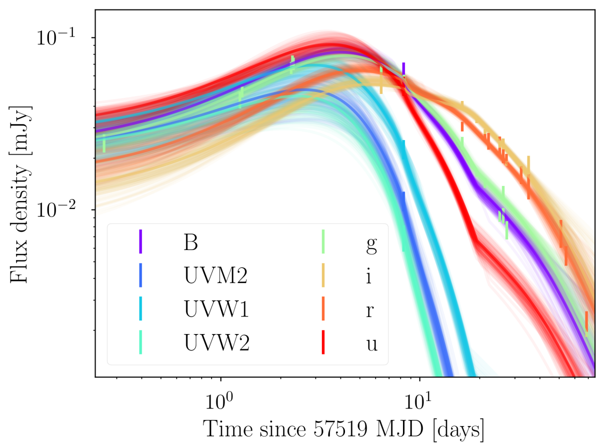

Fig. I.1. Fitted multi-band light curve for iPTF16asu. The solid lines indicate the light curve from the model with the highest likelihood in each band, while the shaded area indicates the 90% credible interval.

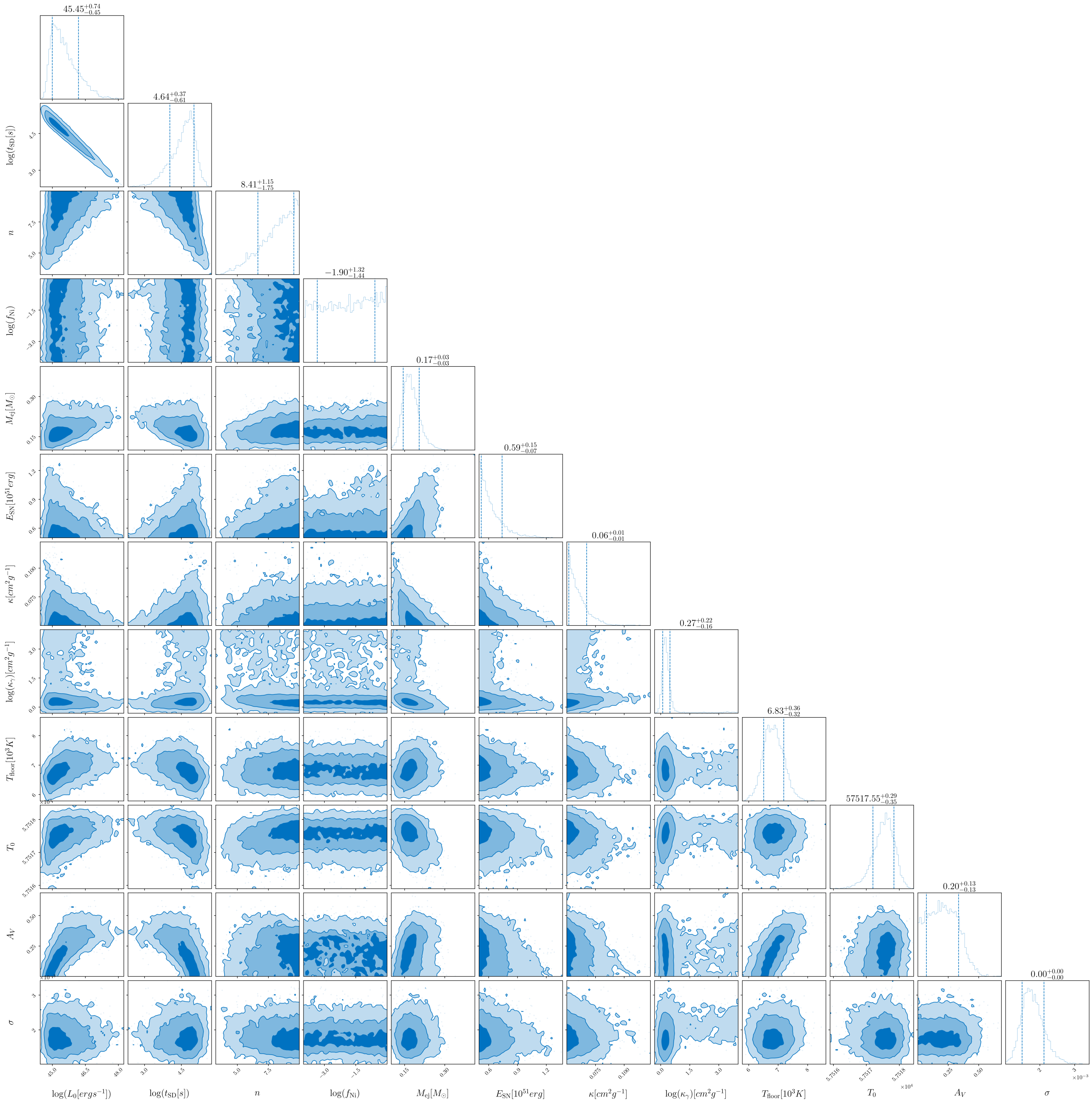

Fig. I.2. Posterior distribution of key physical parameters inferred by the light curve fit shown in Fig. I.1. Median values and 1σ uncertainties are given above each parameter.